



HAL
open science

Debris-Flow Process Controls on Steepland Morphology in the San Gabriel Mountains, California

William Struble, Luke Mcguire, Scott Mccoy, Katherine Barnhart, Odin Marc

► **To cite this version:**

William Struble, Luke Mcguire, Scott Mccoy, Katherine Barnhart, Odin Marc. Debris-Flow Process Controls on Steepland Morphology in the San Gabriel Mountains, California. *Journal of Geophysical Research: Earth Surface*, 2023, 128 (7), 10.1029/2022JF007017 . hal-04187895

HAL Id: hal-04187895

<https://hal.science/hal-04187895>

Submitted on 7 Dec 2023

HAL is a multi-disciplinary open access archive for the deposit and dissemination of scientific research documents, whether they are published or not. The documents may come from teaching and research institutions in France or abroad, or from public or private research centers.

L'archive ouverte pluridisciplinaire **HAL**, est destinée au dépôt et à la diffusion de documents scientifiques de niveau recherche, publiés ou non, émanant des établissements d'enseignement et de recherche français ou étrangers, des laboratoires publics ou privés.

Copyright

JGR Earth Surface

RESEARCH ARTICLE

10.1029/2022JF007017

Key Points:

- Steepland morphology in the San Gabriel Mountains, California, corresponds with catchment-averaged erosion rates
- A landform evolution model with an incorporated debris-flow process law reproduces relationships between morphology and erosion rate
- Modeled fluvial erosion outpaces debris-flow incision upstream from the transition between colluvial valleys and concave channels

Supporting Information:

Supporting Information may be found in the online version of this article.

Correspondence to:

W. T. Struble,
wstruble@arizona.edu

Citation:

Struble, W. T., McGuire, L. A., McCoy, S. W., Barnhart, K. R., & Marc, O. (2023). Debris-flow process controls on steepland morphology in the San Gabriel Mountains, California. *Journal of Geophysical Research: Earth Surface*, 128, e2022JF007017. <https://doi.org/10.1029/2022JF007017>





Received 29 NOV 2022

Accepted 12 JUL 2023

Author Contributions:

Conceptualization: William T. Struble, Luke A. McGuire, Scott W. McCoy, Katherine R. Barnhart, Odin Marc
Formal analysis: William T. Struble, Luke A. McGuire, Scott W. McCoy, Katherine R. Barnhart
Writing – review & editing: William T. Struble, Luke A. McGuire, Scott W. McCoy, Katherine R. Barnhart, Odin Marc

Debris-Flow Process Controls on Steepland Morphology in the San Gabriel Mountains, California

William T. Struble¹ , Luke A. McGuire¹, Scott W. McCoy² , Katherine R. Barnhart³ , and Odin Marc⁴ 

¹Department of Geosciences, University of Arizona, Tucson, AZ, USA, ²Department of Geological Sciences and Engineering, University of Nevada, Reno, Reno, NV, USA, ³U.S. Geological Survey Geologic Hazards Science Center, Golden, CO, USA, ⁴Géosciences Environment Toulouse (GET), UMR, CNRS, IRD, CNES, UPS, Observatoire Midi-Pyrénées, Toulouse, France

Abstract Steep landscapes evolve largely by debris flows, in addition to fluvial and hillslope processes. Abundant field observations document that debris flows incise valley bottoms and transport substantial sediment volumes, yet their contributions to steepland morphology remain uncertain. This has, in turn, limited the development of debris-flow incision rate formulations that produce morphology consistent with natural landscapes. In many landscapes, including the San Gabriel Mountains (SGM), California, steady-state fluvial channel longitudinal profiles are concave-up and exhibit a power-law relationship between channel slope and drainage area. At low drainage areas, however, valley slopes become nearly constant. These topographic forms result in a characteristically curved slope-area signature in log-log space. Here, we use a one-dimensional landform evolution model that incorporates debris-flow erosion to reproduce the relationship between this curved slope-area signature and erosion rate in the SGM. Topographic analysis indicates that the drainage area at which steepland valleys transition to fluvial channels correlates with measured erosion rates in the SGM, and our model results reproduce these relationships. Further, the model only produces realistic valley profiles when parameters that dictate the relationship between debris-flow erosion, valley-bottom slope, and debris-flow depth are within a narrow range. This result helps place constraints on the mathematical form of a debris-flow incision law. Finally, modeled fluvial incision outpaces debris-flow erosion at drainage areas less than those at which valleys morphologically transition from near-invariant slopes to concave profiles. This result emphasizes the critical role of debris-flow incision for setting steepland form, even as fluvial incision becomes the dominant incisional process.

Plain Language Summary Steep landscapes evolve due to erosion by debris flows—sediment-rich slurries that transport abundant wood and other debris—in addition to erosion by rivers and sediment transport on hillslopes. Although debris flows have long been recognized for their ability to erode channels and transport sediment, quantifying how they set the form of steeplands has remained a challenge. We use a landform evolution model that includes debris-flow bedrock erosion to produce synthetic landscapes that exhibit similar patterns in valley-bottom slope as those observed in the San Gabriel Mountains, California. Notably, we observe that the drainage area where simulated erosion by rivers begins to exceed that by debris flows does not correspond with the drainage area where the form of valley bottoms exhibits a transition. Rather, river incision outpaces incision by debris flows at drainage areas smaller than the morphologic transition point, implying that even as debris-flow incision decreases in magnitude relative to river erosion, debris flows still have an outsized ability to dictate the morphology of steep landscapes.

1. Introduction

Landscapes evolve through the interplay of climate and tectonics (e.g., Whittaker, 2012; Wobus et al., 2006). Bedrock valley networks act as conduits through which signals of baselevel propagate upstream, eventually to the hillslopes, which correspondingly adjust their sediment flux and form (Crosby & Whipple, 2006; Gilbert, 1877, 1909; Howard, 1994; Mudd, 2017; Roering et al., 1999). In response to more rapid uplift rates, bedrock rivers steepen and soil-mantled hillslopes develop increased hilltop convexity (e.g., Hurst et al., 2012; Kirby & Whipple, 2001). At the uppermost reaches of valley networks at low drainage areas, steepland valley bottoms commonly exhibit gradients that become nearly constant with decreasing drainage area (Montgomery & Foufoula-Georgiou, 1993). These near-constant valley-bottom slopes grade downstream into concave-up,

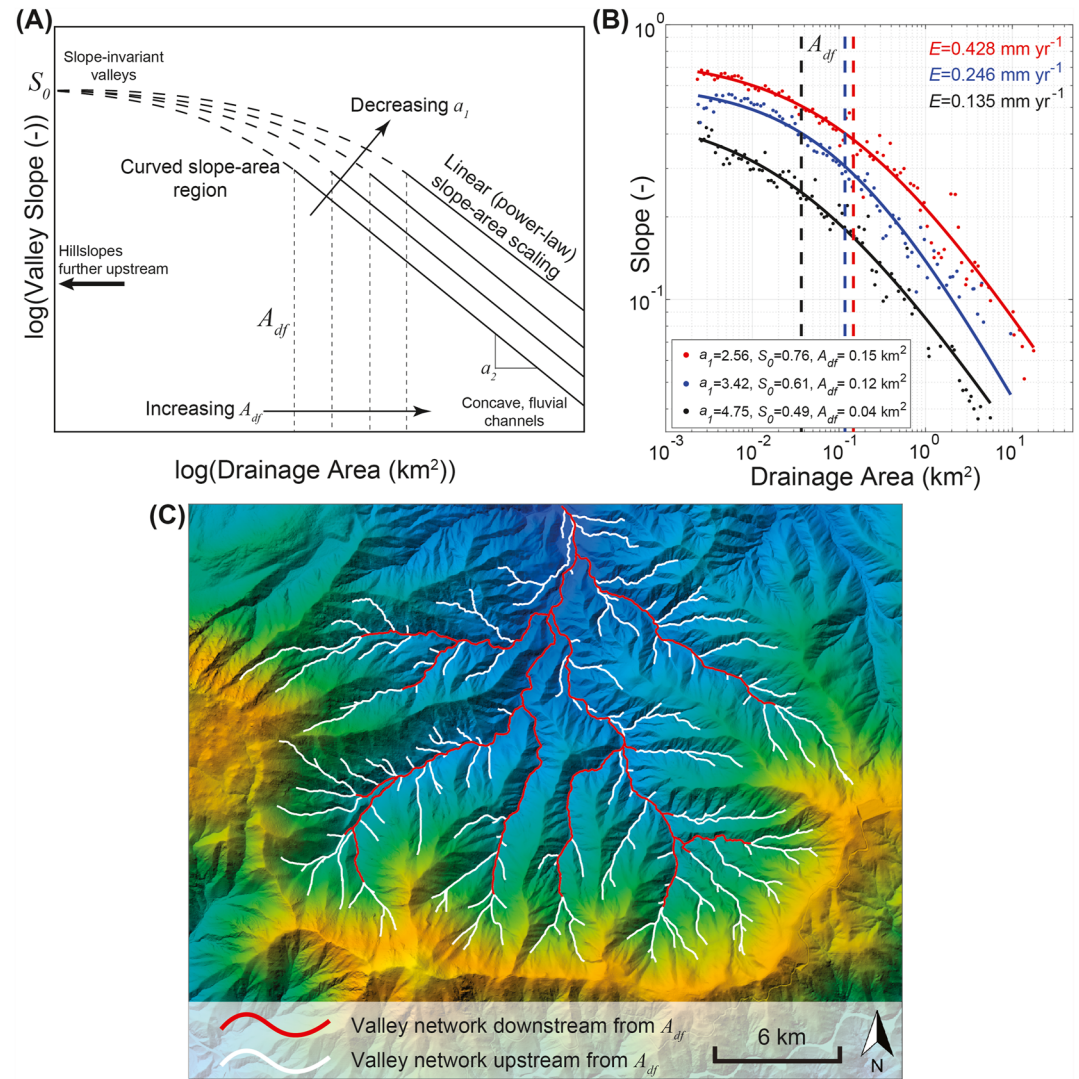


Figure 1. Topographic signatures of debris flows. (a) Schematic slope-area plot for fluvial and steep-land valley bottoms, for the case of constant S_0 . At high drainage areas where fluvial channels are located, power-law scaling between channel slope and drainage area predominates. The slope in log-log space of these channels is the channel concavity, expressed in Equations 1 and 2 as a_2 . As drainage area decreases, valley-bottom slopes approach a constant value, resulting in characteristically curved slope-area data. Decreasing values of a_1 and increasing A_{df} correspond with faster uplift rates (this study; DiBiase et al., 2012; Neely & DiBiase, 2023; Penserini et al., 2017), reflecting a downstream lengthening of the debris-flow network. Note that S_0 may also vary with uplift rate, but it is kept constant here for simplicity. Figure inspired by Penserini et al. (2017). (b) Example slope-area plots from the San Gabriel Mountains (SGM) over a range of erosion rates. Note increasing S_0 and A_{df} and decreasing a_1 as erosion rate increases. (c) Example watershed from the SGM. Valley bottoms upstream from A_{df} are colored white, corresponding to dashed lines in (a), while channels downstream from A_{df} are colored red, corresponding to solid lines in (a).

fluviably carved channels, which results in characteristically curved plots of slope and drainage area in log-log space (Figure 1).

Here, we define “channels” and “valleys” as distinct. Both channels and valleys have an axis of concentrated erosion (i.e., a channel bed or convergent valley bottom). Channels, however, have definable banks and indicators of fluvial incision (e.g., fluting, potholes, sorted sediment), whereas valley bottoms generally lack these features, occur upstream from fluviably incised reaches, and may be filled by poorly sorted hillslope-derived sediments that accumulate between debris-flow events. Most importantly, we distinguish channels as exhibiting power-law slope-area scaling, while valley bottoms deviate from such a relationship. We avoid attaching any genetic or process terms to valley bottoms. For example, colluvial valleys (e.g., Bisson et al., 2006; Lague & Davy, 2003)

imply hillslope processes, and debris-flow valleys (e.g., Penserini et al., 2017; Stock & Dietrich, 2003) suggest that debris flows are predominant for the entire valley length; therefore, we simply refer to them throughout the paper as steepland valleys and/or valley bottoms.

Curved slope-area data have been proposed to represent a topographic signature of debris flows (Figure 1; Montgomery & Foufoula-Georgiou, 1993; Stock & Dietrich, 2003), indicating the predominance of debris-flow erosion at low drainage areas. Indeed, debris flows contribute to erosion and sediment flux in steep headwater valley bottoms (Dietrich et al., 2003; Hsu et al., 2008; McCoy, 2015; McCoy et al., 2013; Sklar & Dietrich, 2001; Stock & Dietrich, 2003, 2006), and there is evidence that the downstream extent and length of steepland valleys may correlate with catchment-averaged erosion rates (DiBiase et al., 2012; Neely & DiBiase, 2023; Penserini et al., 2017; Stock & Dietrich, 2003). Nevertheless, quantitative relationships linking the morphology of these steepland valley networks to tectonic information such as the uplift rate are limited (Neely & DiBiase, 2023; Penserini et al., 2017) and remain elusive in general.

The idea that one could invert topographic form for process and boundary conditions has received substantial attention over the past few decades because landforms are known to adjust their morphology to conform to baselevel conditions. For example, geomorphic transport laws (GTLs) are analytical formulations that describe how surface processes respond and adjust landscape form to tectono-climatic boundary conditions (Dietrich et al., 2003). GTLs have been formulated to quantify incision in bedrock rivers due to fluid shear stresses and saltation/abrasion by sediment (Lague, 2014; Sklar & Dietrich, 2004; Whipple & Tucker, 1999) as well as to account for changes in disturbance-driven sediment flux on hillslopes as their gradient and hilltop convexity adjust to baselevel perturbations (Mudd & Furbish, 2007; Roering et al., 2001, 2007). Steepland valley networks, however, exhibit topographic forms that deviate from those produced by GTLs formulated for hillslopes and bedrock rivers. Specifically, the emergence of curved slope-area data at low drainage areas is a signature that existing hillslope and fluvial GTLs fail to adequately reproduce in steeplands (Figure S1 in Supporting Information S1; Stock & Dietrich, 2003).

GTLs focused on fluvial and hillslope processes have been extensively applied to infer information about climate and tectonics from landforms (e.g., Kirby & Whipple, 2001; Roering, 2008; Roering et al., 2007; Whipple & Tucker, 1999; Wobus et al., 2006). In contrast, similar attempts to quantify the contribution of debris flows to the evolution of steep valley networks have been limited (Stock & Dietrich, 2003, 2006). Stock and Dietrich (2006) formulated a possible debris-flow incision model, but they also emphasized the importance of improving parameterizations for debris-flow dynamics within landscape evolution models to work toward a validated debris-flow GTL. Some works have found that it is possible to produce longitudinal profiles with slope-invariant steepland valley bottoms by using modified versions of fluvial GTLs such as the stream power incision model that incorporates episodic fluvial floods (e.g., DiBiase & Whipple, 2011; Lague, 2014; Lague & Davy, 2003), by placing steep valleys under the control of hillslope processes (e.g., DiBiase et al., 2012; Ouimet et al., 2009), or including stochastic bedrock landsliding in landscape evolution models (e.g., Campforts et al., 2022). Other processes that may result in deviations from power-law slope-area scaling include lower entrainment thresholds required to transport sediment at steep slopes and low drainage areas (e.g., Lamb et al., 2008; Prancevic et al., 2014; Recking, 2009), rapid weathering on steep slopes as topographic stresses produce bedrock fractures (e.g., Li & Moon, 2021; Moon et al., 2017; Neely & DiBiase, 2020; St. Clair et al., 2015), and downstream changes in the width of geomorphically effective flows, including water-dominated floods and debris flows (Alessio et al., 2021; Neely & DiBiase, 2023; Yanites, 2018). In contrast, since Stock and Dietrich (2006), there has been little progress explicating the role of debris flows as geomorphic agents, and basic questions remain about the combined effects of fluvial and debris-flow erosion on the form of steepland valley bottoms and channels and the capability of debris-flow GTLs within landscape evolution models to reproduce this curved slope-area signature. Here, through model experiments and terrain analyses in the San Gabriel Mountains (SGM), California, USA, a landscape where debris-flow processes have been extensively studied, we will address three specific questions that aim to clarify the contributions of debris flows to steepland valley evolution: (a) How does the morphology of steady-state steepland valley networks systematically vary with uplift rate? (b) Can we place additional constraints on the general form of a recently proposed debris-flow GTL? (c) Could the locations of morphologic transitions (i.e., steepland valley bottoms to concave, fluvial channels) be collocated with changes in process dominance (i.e., debris-flow to fluvial incision)?

1.1. Linking Landscape Process With Form

In steep landscapes, the downstream transition of steepland valley bottoms to concave-up channels that exhibit a power-law relationship between valley-bottom slope and drainage area produces curved slope-area data in log-log space (Figure 1). Stock and Dietrich (2003) derived a functional form for this nonlinear relationship between valley-bottom slope, S , and drainage area, A , given as

$$S = \frac{S_0}{1 + a_1 A^{a_2}}, \quad (1)$$

where a_2 is the slope in log-log space at large drainage areas of the linear, power-law portion of the slope-area plot, akin to fluvial concavity, S_0 is the valley-bottom slope at low drainage areas, and a_1 (units of $1/(\text{length}^2)^{a_2}$) describes the curvature of the slope-area data, which can also be conceptualized as the abruptness of the down-valley transition from nearly constant-slope valley bottoms to power-law slope-area scaling (Figure 1). An alternative formulation of Equation 1, utilized by McGuire et al. (2022), quantifies the curved slope-area relationship with a critical drainage area parameter. Specifically, this formulation can be expressed as

$$S = \frac{S_0}{1 + \left(\frac{A}{A_{df}}\right)^{a_2}}, \quad (2)$$

where A_{df} represents the most upstream extent of power-law slope-area scaling and the drainage area at which gradient begins transitioning to slope-invariant valley bottoms (Figure 1). Comparing Equations 1 and 2, we find that $A_{df} = a_1^{-1/a_2}$. Importantly, A_{df} has the same units as drainage area (length^2) and perhaps provides a more conceptually intuitive description of down-valley changes in longitudinal profiles than does a_1 . That is, larger A_{df} corresponds with steepland valleys that extend farther downstream to larger drainage areas. Importantly, A_{df} is *not* the location at which disturbance-driven (i.e., diffusive) hillslope processes transition to shear-driven erosion by water or debris flows, which would amount to hillslope length. The hillslope-valley transition is located upstream from A_{df} at the uppermost reaches of steepland valley bottoms. A_{df} , rather, defines the *downstream* extent of these valleys (Figure 1).

Penserini et al. (2017) demonstrated in the Oregon Coast Range that a_1 scales inversely with erosion rate and suggested that decreasing values of a_1 , that is, more spatially extensive steepland valley networks (i.e., larger A_{df}), correspond with faster uplift rates in the core of the Oregon Coast Range. Similarly, McGuire et al. (2022) utilized empirical relationships of bulk debris-flow properties (e.g., depth, volume) as a function of landscape position (i.e., drainage area; Rickenmann, 1999) coupled with one possible debris-flow GTL (which we discuss below in Section 1.2) and noted that A_{df} increases as a function of uplift rate once the valley profile reaches a steady state. In the SGM, DiBiase et al. (2012) and Neely and DiBiase (2023), respectively, noted that steepland valleys were longer and A_{df} is larger in more rapidly eroding catchments than in more slowly eroding catchments. Neely and DiBiase (2023), however, implicated sediment grain size and the relative ability of debris flows and fluvial floods to transport sediment as being more important for setting the location of A_{df} than uplift rate alone. Nonetheless, Equations 1 and 2 not only capture the topographic signature of a specific process but additionally provide a framework for a morphologic proxy that can be used to extract tectonic information from topography. However, further clarification of potential relationships between process and form in steep landscapes is needed to inform the use of A_{df} (and a_1) as a morphologic proxy for uplift rate and to construct a debris-flow GTL.

In a similar fashion to A_{df} , McGuire et al. (2022) utilized their 1-dimensional (1D) model to analytically solve for steepland valley-bottom slope, S_0 . They observed that S_0 should increase with faster uplift rates in a less-than-linear fashion (exponent <1) for cases where fluvial incision is minimal, which may occur at the uppermost reaches of steepland valleys. Although the nature of the relationship between uplift rate and S_0 in natural landscapes is generally unclear, observations from Neely and DiBiase (2023) indicate that S_0 may exhibit a positive, roughly linear correlation with erosion rate at modest erosion rates and potentially reach a threshold S_0 value at more rapid erosion rates. Because landscape evolution models should be able to reproduce observed relationships between key forcing mechanisms (e.g., uplift) and landscape morphology, further quantifying the relationship between A_{df} , S_0 , and erosion rate could also help with the formulation and testing of a debris-flow GTL.

1.2. Formulating a Debris-Flow Geomorphic Transport Law

At low drainage areas, sediment transport by fluvial processes is limited by low discharge, and large flood events are often necessary to transport sediment and incise bedrock (e.g., Cook et al., 2013; DiBiase & Whipple, 2011;

Lague, 2014; Sklar & Dietrich, 2001; Stock et al., 2005; Turowski et al., 2008). Lamb et al. (2008) noted that higher critical Shields stresses are required to transport sediment as channel slope increases, and Prancevic et al. (2014) further demonstrated that at high slopes and Shields stresses, channel sediment fails *en masse* after a threshold discharge is reached. Hence, in steep channel networks where drainage area is too low to accumulate sufficient discharge for floods to transport sediment and where channel roughness increases relative to flow depth (Lamb et al., 2008), incision of the bed must occur via failure and fluidization of bed material (Prancevic et al., 2014). These observations, coupled with observations of bedrock erosion by debris flows (Hsu et al., 2014; McCoy et al., 2013; Stock & Dietrich, 2003, 2006), further indicate that debris flows predominate at low drainage areas and may be responsible for a substantial proportion of bedrock incision in these locations.

Field observations and experimental studies of laboratory and instrumented natural channels have demonstrated that debris flows erode bedrock largely due to the impact of transported grains on the channel bed (Hsu et al., 2008, 2014; Iverson, 1997; McCoy et al., 2010, 2013). For example, Hsu et al. (2008, 2014) observed in a series of experiments in rotating drums of various sizes that debris-flow incision could be described as a function of inertial normal stress, likely owing to large force excursions from the time-averaged basal normal stress (Hsu et al., 2014; McCoy et al., 2013). Granular snouts with little-to-no pore fluid pressure consolidate at the front of debris flows and are followed by water-dominated tails with high pore pressures (Iverson, 1997; McCoy et al., 2010). Within natural channels, Stock and Dietrich (2006) suggested that erosion by debris flows is highest during the passage of these sediment-rich debris-flow snouts, although McCoy et al. (2013) noted in an instrumented channel in the Rocky Mountains that the distribution of basal forces was similar between the solids-rich granular surge fronts of debris flows and their water-rich tails. However, although abundant work demonstrates that debris flows are important agents of valley-bottom erosion and sediment flux in steeplands, it remains an ongoing challenge to constrain the effects of bulk debris-flow properties on their erosive power over geologic timescales, particularly as modulated by valley-bottom slope and debris-flow depth within the framework of a GTL. Stock and Dietrich (2006) put forth one possible debris-flow GTL and suggested that over geologic timescales, bedrock incision by debris flows is a result of inertial normal stresses of debris-flow particle impacts on the channel bed as well as other factors such as valley-bottom slope, bedrock weathering, debris-flow recurrence interval, and downstream bulking of sediment. While their 1D model was able to reproduce the curved slope-area data indicative of debris flows, their equations contain many parameters that require site-specific calibration.

Recently, McGuire et al. (2022) presented a 1D model to simulate valley and channel longitudinal profiles that includes a method to compute spatial variations in bulk debris-flow properties throughout the valley network and relate these to debris-flow incision rates. More specifically, they proposed one potential family of debris-flow incision laws wherein the debris-flow erosion rate at a point scales with debris-flow depth and valley-bottom slope, each raised to some empirical exponent. The general form of this family of debris-flow incision laws was motivated by observations that grain-scale bed impact forces increase with flow depth (McCoy et al., 2013) and past work indicating debris-flow erosion scales with inertial stress (Hsu et al., 2008, 2014), which can be cast in terms of flow depth and depth-averaged velocity. Viewing slope as a proxy for flow velocity (Silbert et al., 2001), it is reasonable to postulate a debris-flow incision law based on slope and flow depth. Combined with the stochastic-threshold stream power incision model (DiBiase & Whipple, 2011; Lague, 2014), McGuire et al. (2022) used their model to explore the effects of debris-flow processes on valley form. Their model, while not applied to a specific landscape, reproduced curved slope-area data with morphometrics (A_{df} , a_2 , S_0 , etc.) that are consistent with natural landscapes when certain conditions are met for the empirical exponents in the debris-flow incision law. Placing additional constraints on the exponents in the debris-flow incision law, however, requires more detailed comparisons between modeled and observed topography in landscapes where erosion rates and other debris-flow process parameters can be estimated.

Here, we aim to constrain the form of the debris-flow incision law proposed by McGuire et al. (2022) by applying their model to the SGM. We accomplish this by reproducing longitudinal valley profiles that are consistent with those from catchments in the SGM, including how valley profile form varies with uplift rate. The SGM provide an ideal landscape for these analyses due to past studies that provide a wealth of information about catchment-averaged erosion rates (DiBiase et al., 2010), debris-flow processes (DiBiase & Lamb, 2020; Gartner et al., 2014; Kean et al., 2011; Lamb et al., 2011; Lavé & Burbank, 2004; McGuire et al., 2017), and steepland morphology (DiBiase et al., 2010, 2012; Groh & Scheingross, 2021; Heimsath et al., 2012; Neely & DiBiase, 2023; Neely et al., 2019). As we later show, steep valleys in the SGM do not have one characteristic

longitudinal profile, but instead show a range of morphologies that vary as a function of uplift rate, a more difficult characteristic for a model of debris-flow incision to successfully reproduce.

1.3. Morphologic and Process Transitions

Although curved slope-area plots have been postulated as a topographic signature of debris flows, whether this morphologic signature provides information on the location (e.g., a drainage area) at which fluvial and debris-flow processes switch in predominance is unclear. Assessing process dominance in various portions of the landscape is critical to developing conceptual as well as mathematical models for landscape evolution, including determinations about which GTLs may be more appropriate for different applications (Dietrich et al., 2003). Substantial work has been devoted to investigating morphologic and process transitions in landscapes where fluvial and diffusive processes dominate. For example, fluvial channel heads serve as the uppermost extent of fluvial drainage networks. As such, objective mapping of channel heads is important for identifying where diffusive processes give way to fluvial incision and how exogenic processes (e.g., uplift rate, climate, vegetation) dictate this location (Clubb et al., 2014; Hergarten et al., 2016; Pelletier, 2013; Pelletier et al., 2016; Perron et al., 2008). Channel head identification is additionally useful for mapping the fluvial drainage network and its tributaries (Lashermes et al., 2007; Passalacqua et al., 2010) and for identifying the base level, and by extension relief and length, of soil-mantled hillslopes (Grieve et al., 2016; Perron et al., 2008; Roering et al., 2007). However, in steep landscapes where debris flows are common, it is not clear where a downstream transition from debris-flow to fluvial process dominance may occur and how this process transition may correspond with any morphologic transition. As such, a model that includes a debris-flow GTL, such as that which we present here, is beneficial to better inform our understanding of the relative importance of fluvial and debris-flow incision throughout steep valley networks and how process and morphologic transitions may or may not be collocated.

Given A_{df} , as defined in Equation 2, quantifies a morphologic transition from steepland valley bottoms to concave channels, it is intuitive to ask whether it additionally corresponds with a switch in process dominance. The presence or absence of debris-flow deposits has been used to postulate where the transition from debris-flow to fluvial incisional predominance occurs (DiBiase et al., 2012; Stock & Dietrich, 2003, 2006). However, it remains ambiguous whether debris-flow deposits provide quantitative information on dominant incisional processes and whether the drainage area at which process transitions occur (i.e., where fluvial incision exceeds that from debris flows) also corresponds with the drainage area at which morphologic transitions occur (i.e., A_{df}). For example, DiBiase et al. (2012) noted in the SGM that debris flows often travel well-downstream from the drainage area at which steepland valleys transition to concave profiles, yet the morphologic effect of debris flows at these larger drainage areas appears minor relative to fluvial incision.

Here, we utilized A_{df} to demarcate the approximate location of the morphologic transition from steepland valley bottoms to concave channels. However, although A_{df} corresponds with a single drainage area, it does not strictly indicate that the debris flow-fluvial *process* transition is correspondingly abrupt. Thus, although it may be tempting to equate a drainage area that demarcates a transition between steepland valley bottoms and concave channels with a concomitant switch from debris-flow to fluvial process predominance (or perhaps with a characteristic debris-flow runout distance), we interpret A_{df} as the approximate location of a transitional zone along the curved slope-area function (Figure 1). As such, it is unclear how A_{df} may correspond with down-valley process transitions. In order to evaluate whether process transitions equate with their morphologic counterparts, we compare A_{df} of modeled valley profiles (Section 1.2) to the drainage area at which modeled incision by fluvial processes exceeds that of debris flows when moving downstream.

2. Study Area

The SGM are situated within the Transverse Ranges of southern California along a restraining bend in the San Andreas Fault, which results in a region of transpression and subsequent rapid uplift along numerous faults (Blythe et al., 2000; Petersen & Wesnousky, 1994). Transpression additionally produces a spatial gradient in uplift rates, with a greater proportion of dip slip and higher uplift and erosion rates in the east of the range. Long-term denudation rates measured from thermochronology generally bracket ~ 0.1 – 1.0 mm yr⁻¹ (Blythe et al., 2000; Lavé & Burbank, 2004; Spotila et al., 2002), and erosion rates measured with cosmogenic ¹⁰Be span from 0.035 to 1.1 mm yr⁻¹ (Figure 2a; DiBiase et al., 2010). Although denudation varies spatially throughout the

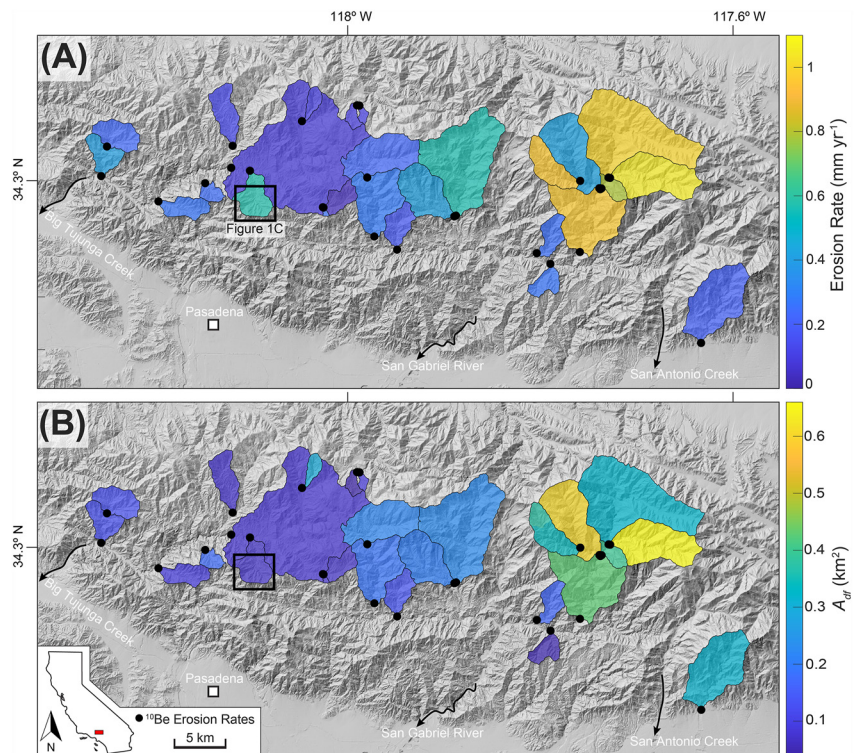


Figure 2. Map of catchments in the San Gabriel Mountains utilized in this study. (a) Catchment-averaged erosion rates used in this study. (b) Map of A_{df} for studied catchments. Higher A_{df} values in the eastern portion of the study area correspond with faster erosion rates in (a). Black dots are sample locations for cosmogenic ^{10}Be erosion rates (DiBiase et al., 2010). Black box corresponds to the outline of Figure 1c. Catchment details are listed in Table 1. See Figure S6 in Supporting Information S1 for map of a_1 .

SGM, broad agreement between ^{10}Be erosion rates and thermochronologically derived uplift rates, which integrate over longer timescales, coupled with the general lack of conspicuous knickpoints, has led to the hypothesis that some morphotectonic blocks in the SGM are in steady state (DiBiase et al., 2010; Lavé & Burbank, 2004). In other regions of the SGM, however, a suite of knickpoints and some discrepancies between thermochronometric denudation rates and cosmogenic erosion rates indicate recent landscape transience and disequilibrium (DiBiase et al., 2015), although some knickpoints may result from autogenic formation processes (Groh & Scheingross, 2021).

The SGM are lithologically composed primarily of Mesozoic granitic rocks that are relatively homogenous throughout the range, particularly within the catchments that we study here (Morton & Miller, 2006; Yerkes & Campbell, 2005). The SGM are characterized by warm, dry summers and mild, moist winters with mean annual precipitation of $\sim 0.7\text{--}1.0\text{ m yr}^{-1}$ (PRISM Climate Group, 2021). Vegetation is dominated by chaparral, particularly at lower elevations where fires have occurred every two to three decades over the past century, but likely every ~ 100 years prior to European colonization (Lamb et al., 2011; Lavé & Burbank, 2004; Parson et al., 2010; Swanson, 1981). Soils are patchy and relatively thin ($<0.5\text{--}1\text{ m}$), particularly on steep slopes (Heimsath et al., 2012; Kean et al., 2011; Rengers et al., 2020).

3. Methods

We investigated the contributions of debris flows to landscape evolution through a combination of topographic analysis and landform evolution modeling. Specifically, we mapped the morphologic properties of steady-state steep-land networks in the SGM. We parameterized debris-flow volume for a 1D landform evolution model by utilizing an empirical debris-flow volume model, originally developed in the Transverse Ranges and applied effectively in the SGM (Gartner et al., 2014; Rengers et al., 2020). We then conducted a numerical experiment with a 1D landform evolution model. The numerical experiment was designed to constrain the parameter values

in a debris-flow incision law needed to reproduce the observed relationship between longitudinal valley morphology and uplift rate in the SGM. Finally, we compared morphologic transitions as quantified by A_{df} to the drainage area at which fluvial incision outpaces debris-flow incision.

3.1. Morphometric Analysis

We used 10-m digital elevation models (DEMs; U.S. Geological Survey, 2019) and TopoToolbox (Schwanghart & Scherler, 2014) to map stream networks in 29 watersheds, a subset of SGM catchments with existing ^{10}Be catchment-averaged erosion rates (DiBiase et al., 2010). Although 1-m lidar data are available for our study area, we found that using 10-m DEMs produced slope-area plots that were consistent with 1-m lidar data and avoided flow-routing complications introduced by the presence of roads that are more apparent in high-resolution lidar data. We excluded catchments from the existing ^{10}Be data set (21 of the 50 watersheds in DiBiase et al. (2010)) from our analysis if they exhibited signs of disequilibrium, particularly conspicuous knickpoints in the channel longitudinal profiles, including those that may be associated with lithologic contacts. We additionally did not consider small catchments that do not exhibit curved slope-area data, corresponding to watersheds with drainage areas $< \sim 0.1\text{--}1\text{ km}^2$, where fluvial processes are likely too limited to imprint conspicuous power-law slope-area scaling. We mapped valley networks using a threshold drainage area, A_0 , of $10,000\text{ m}^2$. This drainage area is sufficiently large to ensure we are downstream from hillslopes where disturbance-driven diffusive processes, which are not considered in our model, are dominant (Figure 1). Although the drainage area at which valley heads initiate may exhibit a systematic relationship with uplift and erosion rate, as indicated by relationships between drainage density and erosion rate for fluvial channels (Clubb et al., 2016), objective mapping of the hillslope-steepland valley transition is beyond the scope of this work. We confirmed, however, that variations in A_0 have little effect on observed relationships between erosion rate and A_{df} and S_0 (and a_1) (Figures S2 and S3 in Supporting Information S1), as long as A_0 is sufficiently large to fall downstream from the hillslopes.

We binned slope-area data for each catchment with 100 logarithmically spaced bins between the minimum and maximum drainage areas and collected median drainage area and mean gradient in each bin. These binning and averaging techniques are consistent with other recent studies (e.g., Neely & DiBiase, 2023; Penserini et al., 2017). Slope-area plots and longitudinal profiles for each catchment can be found in Supporting Information S1 (Figures S4 and S5). Although binning slope-area data smooths over signals in catchments that are often important for topographic analysis of some landscape features (i.e., knickpoints), we purposefully selected catchments free from indications of disequilibrium to ensure that the signal of morphologic transitions is preserved. We recognize, however, that additional morphologic signatures of debris-flow processes, such as stepped longitudinal profiles (Stock & Dietrich, 2006), may be obscured by utilizing binned slope-area data and that isolating individual debris-flow channels may also provide a clearer indication of which valley bottoms are debris-flow dominated (e.g., Mueting et al., 2021). Although these signatures are worthy of ongoing and future attention, particularly within a 2-dimensional (2D) topological framework, we focused on debris-flow signatures that appear across catchments on a landscape scale and have received the most attention in past studies (e.g., Penserini et al., 2017). Finally, we used least squares regression to fit Equation 2 to the slope-area data for each catchment of interest, from which we extracted A_{df} , S_0 , and a_2 . We additionally calculated a_1 by utilizing least square regression to fit Equation 1 to slope-area data from SGM catchments (Figure S6 in Supporting Information S1); however, because most recent studies preferentially utilize A_{df} to examine the relationship between erosion rate and debris-flow catchment morphology (e.g., McGuire et al., 2022; Neely & DiBiase, 2023), we similarly emphasize results for A_{df} .

We correlated measured A_{df} and S_0 to catchment-averaged erosion rates, E , in the SGM. These observed relationships provide quantitative information that we used to assess the performance of the landform evolution model. To aid comparison of relationships between morphology and erosion rate that we observed in the SGM to model results laid out in the next section, we bootstrapped 1,000 linear and power-law fits to both $A_{df} \sim E$ and $S_0 \sim E$, respectively (Figure 3; Figure S7 in Supporting Information S1 for $a_1 \sim E$). For each bootstrapped linear or power-law fit, we iteratively sampled with replacement the SGM data 29 times, which is the size of the trimmed SGM ^{10}Be data set. From these 1,000 bootstrapped fits, we identified 95% confidence intervals (Figure 3, Figures S7 and S8 in Supporting Information S1).

3.2. Landform Evolution Model

We used the 1D landform evolution model from McGuire et al. (2022) to test how valley profiles evolve due to the interplay of debris-flow and fluvial processes. The model simulates a bedrock longitudinal valley profile

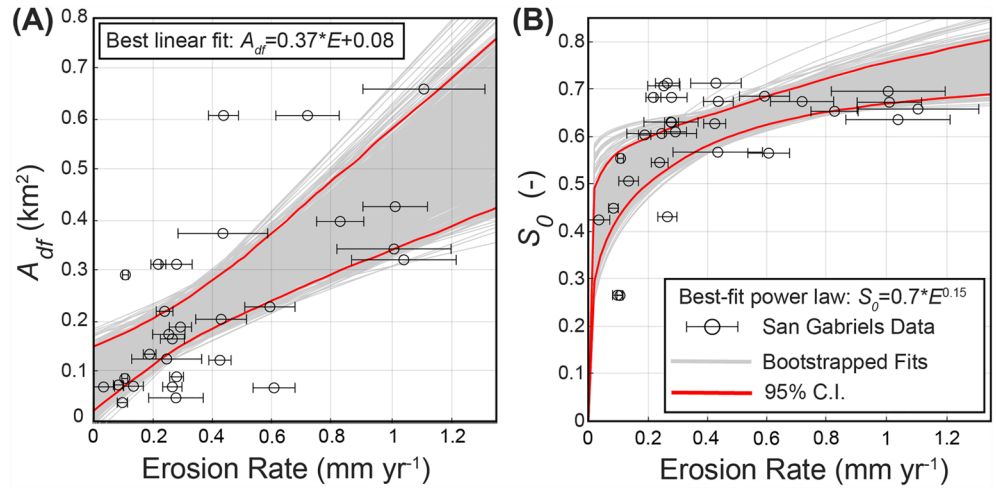


Figure 3. Morphologic data from the San Gabriel Mountains. (a) Catchment A_{df} (black circles) plotted against erosion rate exhibits lower A_{df} at fast erosion rate. (b) Catchment S_0 (black circles) plotted against erosion rate. Gray lines are bootstrapped power-law fits to the morphologic data, and red lines are the 95% confidence intervals for the 1,000 bootstrap fits. In both panels, error bars correspond to erosion rate uncertainty listed in Table 1. See Figure S7 in Supporting Information S1 for a_1 .

with distance from the headwater valley node, x , and elevation, z , through time, t , as it adjusts to uplift, U , fluvial erosion, E_f , and erosion by debris flows, E_{df} , according to

$$\frac{\partial z}{\partial t} = U - E_f - E_{df}. \quad (3)$$

Equation 3 was solved numerically on a grid of uniform spacing, $\Delta x = 5$ m. For time stepping, we used the standard explicit forward Euler method. We computed fluvial erosion utilizing the stochastic-threshold version of the stream power incision model (DiBiase & Whipple, 2011; Lague, 2014), denoted as

$$E_f = K A^{m_s} S^{n_s}, \quad (4)$$

where A is upstream drainage area, S is valley-bottom slope, and K , m_s , and n_s are empirical values that include relationships between discharge and channel width, w , hydraulic geometry and discharge variability, and grain size (Supporting Information S1). S was calculated using explicit first-order upwind differencing, and we calculated A based on a systematic increase of distance from the headwater valley node according to $A = A_0 + 25x^3$, where $A_0 = 10,000$ m², which is the same as the A_0 utilized to map valleys in the SGM. Because this value falls downstream from the hillslope-valley transition and because the model is designed only to simulate changes in the elevation of the bedrock surface through time, we excluded diffusive processes from our 1D modeling framework. We additionally assumed that channel width varies as a function of drainage area, such that

$$w = k_w A^{b_w}, \quad (5)$$

where $k_w = 0.05$ and $b_w = 0.3$ (for drainage area units of m²; DiBiase & Whipple, 2011; Lague, 2014). A full list of parameters used for the stream power model can be found in Supporting Information S1 (Table S1).

The landform evolution model quantifies erosion by debris flows over geologic timescales as a function of bulk debris-flow properties, debris-flow depth, h , and valley-bottom slope, S (McGuire et al., 2022). Specifically, erosion by debris flows at a point along a channel, E_{df} , is defined as

$$E_{df} = k_{df} t_p S^\alpha h^\beta \Theta, \quad (6)$$

where t_p is the passage time of a debris flow, k_{df} is an erodibility coefficient that accounts for bedrock and flow properties (e.g., grain size, lithology) as well as debris-flow frequency, α and β are exponents, and Θ is a threshold factor that reduces incision as a debris flow nears the end of its runout. McGuire et al. (2022) found that particular values of α and β produce valley profiles that are most consistent with natural landscapes. They noted that models

Table 1
San Gabriel Mountains Catchment Characteristics

Sample ID ^a	Lat ^a (°N)	Long ^a (°W)	Erosion rate ^a (mm yr ⁻¹)	k_{sn} ^a (m ^{0.9})	A_{df} (km ²)	S_0 (-)	a_1 (km ^{-2a2})	Relief-area coefficient (f_1) ^b	Relief-area exponent (f_2) ^b
SGB3	34.3114	-118.1219	0.084 ± 0.016	63 ± 6	0.08	0.45	3.58	9.49	0.26
SGB4	34.2781	-118.0266	0.035 ± 0.037	43 ± 1	0.07	0.42	4.21	13.9	0.27
SGB5	34.3302	-118.1209	0.135 ± 0.033	60 ± 1	0.07	0.51	4.09	10.2	0.26
SGB6	34.3284	-118.2504	0.246 ± 0.117	115 ± 4	0.13	0.61	3.64	5.27	0.26
SGB7	34.298	-118.1488	0.253 ± 0.054	106 ± 8	0.18	0.71	3.1	4.36	0.3
SGB9	34.3029	-118.256	0.424 ± 0.037	118 ± 3	0.12	0.63	3.74	9.82	0.29
SGB10	34.2819	-118.1967	0.279 ± 0.023	105 ± 5	0.09	0.63	4.03	7.58	0.29
SGB11	34.2966	-117.7403	0.826 ± 0.079	157 ± 3	0.4	0.65	1.68	9.46	0.3
SGB12	34.242	-117.7621	1.01 ± 0.108	163 ± 2	0.43	0.67	1.62	10.45	0.31
SGB13	34.2967	-117.7425	0.436 ± 0.05	178 ± 4	0.61	0.67	1.35	9.82	0.29
SG118	34.2785	-118.0271	0.265 ± 0.032	43 ± 1	0.07	0.43	4.25	14.69	0.27
SG123	34.352	-118.0496	0.108 ± 0.01	66 ± 2	0.29	0.55	2.37	9.78	0.26
SG131	34.3659	-117.9931	0.098 ± 0.017	29 ± 3	0.04	0.27	7.06	10.45	0.31
SG132	34.3657	-117.9904	0.106 ± 0.01	35 ± 4	0.09	0.27	5.01	12.26	0.28
SG137	34.2723	-117.89	0.591 ± 0.084	154 ± 3	0.23	0.69	2.26	3.48	0.35
SG138	34.2717	-117.8919	0.428 ± 0.085	131 ± 3	0.21	0.71	2.36	3.17	0.37
SG140	34.2427	-117.9504	0.189 ± 0.021	93 ± 6	0.14	0.6	2.86	15.59	0.26
SG141	34.2539	-117.9741	0.292 ± 0.037	126 ± 4	0.19	0.61	2.3	11.26	0.31
SG151	34.3205	-117.8002	0.434 ± 0.15	146 ± 17	0.37	0.57	1.87	16.18	0.27
SG157	34.3057	-117.7313	1.106 ± 0.204	173 ± 5	0.66	0.66	1.29	14.9	0.27
SG158	34.3058	-117.7332	1.039 ± 0.175	145 ± 3	0.32	0.64	1.88	19.1	0.26
SG159	34.2959	-117.7416	0.717 ± 0.106	178 ± 4	0.61	0.67	1.35	11.07	0.28
SG161	34.3029	-117.7623	1.006 ± 0.191	164 ± 7	0.34	0.7	1.94	16.16	0.27
SG162	34.165	-117.6362	0.279 ± 0.052	172 ± 6	0.31	0.68	1.8	13.09	0.29
SG163	34.165	-117.6362	0.218 ± 0.025	172 ± 6	0.31	0.68	1.8	17.8	0.27
SG206	34.2317	-117.7923	0.277 ± 0.091	81 ± 12	0.05	0.63	5.48	13.02	0.29
SG207	34.2408	-117.8065	0.265 ± 0.04	89 ± 3	0.17	0.71	2.68	20.03	0.26
SG0703	34.3091	-118.1027	0.605 ± 0.07	66 ± 3	0.07	0.57	4.62	17.91	0.26
SG0743	34.3043	-117.9818	0.239 ± 0.028	113 ± 5	0.22	0.55	2.03	13.32	0.29

^aAs reported by DiBiase et al. (2010). For k_{sn} , reference concavity is 0.45. ^bSee Figure 4.

that used $\alpha < 3$ and $\beta > 2$ generally performed poorly, but they also found that reproducing curved slope-area plots was insufficient to differentiate among a wide range of potential incision laws, especially without additional controls on model inputs used to parameterize changes in debris-flow volume and likelihood with drainage area. In Equation 6, h represents a characteristic debris-flow depth that can vary along the valley profile. We elaborate on how we determine the parameters in Equation 6 below and k_{df} in Section 3.3.

The landform evolution model of McGuire et al. (2022) uses the empirical debris-flow routing algorithm of Gorr et al. (2022) to calculate spatial variations in debris-flow properties. The routing algorithm determines the travel path of the debris flow from the top of the valley network to its downstream stopping point as well as bulk debris-flow properties along that travel path. Debris-flow properties along the travel path are based on empirical relationships (Rickenmann, 1999) that can be used in conjunction with channel width, w , and slope, S , to estimate flow depth and passage time. Debris flows initiate at the grid cell with the lowest drainage area ($A_0 = 10,000 \text{ m}^2$) in the model domain, corresponding with the headwater valley node. We treated the debris flows as an idealized fluid that has a specified yield strength, τ_y , and we assumed that debris flows stop when basal shear stress,

$\tau = \rho_b g R_h \sin \theta$, is less than τ_y , where $g = 9.81 \text{ m s}^{-2}$ is acceleration due to gravity, $\rho_b = 1,800 \text{ kg m}^{-3}$ is flow bulk density, $R_h = \frac{wh}{w+2h}$ is the hydraulic radius of a rectangular channel, and θ is the slope angle of the valley bottom. Based on calculated h , t_p , and τ throughout the entire model domain, we computed E_{df} in the locations traversed by debris flows.

In natural landscapes, debris-flow volume typically increases as a function of drainage area due to downstream entrainment of bed material (Santi & Morandi, 2013; Santi et al., 2008). We calculated peak debris-flow discharge, Q , as a function of debris-flow volume, V , as

$$Q = c_1 V^{c_2}, \quad (7)$$

where $c_1 = 0.0188$ and $c_2 = 0.790$ are empirical coefficients (Rickenmann, 1999). We elaborate on how we calculate V in the next section. Given that $Q = vvh$, where w is channel width and v is debris-flow velocity expressed as

$$v = \frac{1}{3\mu} \rho_b g h^2 S, \quad (8)$$

where μ is flow dynamic viscosity, we solve for flow depth as

$$h = \left(\frac{3\mu c_1 V^{c_2}}{\rho_b g S w} \right)^{\frac{1}{3}}. \quad (9)$$

Continuing, we recast Equation 9 by utilizing empirical relationships between channel width, w , and drainage area, A , (Equation 5) as

$$h = \left(\frac{3\mu c_1 V^{c_2}}{\rho_b g S k_w A^{b_w}} \right)^{\frac{1}{3}}. \quad (10)$$

Importantly, although the model provides an estimate of debris-flow depth, it does not consider sediment deposited by the debris flow, as we assume that debris-flow deposits are immediately removed by fluvial processes. Passage time of the debris flow, t_p , at each point along the valley profile is expressed as

$$t_p = \frac{V}{Q} = \frac{V}{c_1 V^{c_2}}. \quad (11)$$

The threshold factor, Θ , implies that simulated debris flows are less erosive as they come to rest. It is defined as,

$$\Theta = 1 - \frac{\tau_y}{\tau}. \quad (12)$$

Utilizing Equations 10–12 as well as values for k_{df} , α , and β (Section 3.3), E_{df} was then calculated using Equation 6. Although several parameters are put forth here, the well-constrained nature of debris flows in the SGM limits the number of parameters that require calibration to α , β , and k_{df} .

3.2.1. Debris-Flow Volume Parameterization

Debris flows often grow as they travel downstream and entrain available sediment, leading to a systematic relationship between debris-flow volume and drainage area. Santi and Morandi (2013) observed that a series of power laws describe debris-flow volume in different landscapes of the western United States and Italy following $V = V_0 A^\gamma$, where V_0 and γ are empirical coefficients and exponents, respectively, that vary depending on the landscape. In a sensitivity analysis of the 1D landform evolution model described in the previous section, McGuire et al. (2022) noted that γ has a substantial effect on modeled A_{df} and S_0 , such that an increase in γ , all else equal, results in smaller A_{df} and larger S_0 . In addition, systematic variation of γ with uplift rate can produce different relationships between A_{df} and S_0 and uplift rate than if debris-flow volume is fully independent of uplift rate. Hence, it is necessary to parameterize expected changes in debris-flow volume as a function of drainage area and uplift rate to ensure that modeled relationships between catchment morphology and uplift rate reflect underlying relationships between uplift rate and debris-flow volume. Application of existing data sets that quantify the relationship between debris-flow volume and drainage area in the western United States (e.g., Santi & Morandi, 2013) tends

to produce underestimated volumes in the SGM relative to those measured in the field (Gartner et al., 2014). Hence, we rely on a debris-flow volume model developed specifically using data from the Transverse Ranges of southern California to parameterize debris-flow volume, rather than utilize values of γ that are fit based on data from a range of landscapes.

In our application of the 1D landform evolution model to the steep catchments of the SGM, we assumed that debris flows occur following wildfire. Although debris flows in some landscapes (e.g., Oregon Coast Range) initiate as discrete failures on hillslopes, often in the form of shallow landslides (e.g., Benda, 1990; Iverson, 1997; Schmidt et al., 2001; Stock & Dietrich, 2006), debris flows in the Transverse Ranges primarily initiate during short-duration intense rainfall following wildfire where runoff rapidly entrains sediment (Alessio et al., 2021; Cannon, 2001; Guilinger et al., 2020; Kean et al., 2011, 2013; Lamb et al., 2011; McGuire et al., 2017; Palucis et al., 2021; Rengers et al., 2020). Although debris flows also mobilize from shallow landslides, regardless of recent disturbance by fire, they do not account for a large portion of the sediment budget compared to post-wildfire debris flows in the SGM (Lavé & Burbank, 2004; Rengers et al., 2020). As such, a clear linkage between wildfire and debris-flow initiation in the SGM has led to the formulation of empirical models that describe the volume and likelihood of post-wildfire debris flows as a function of rainfall intensity, burn severity, and topographic parameters (Gartner et al., 2014; Staley et al., 2017).

We parameterized debris-flow volume for the SGM by utilizing the empirical post-wildfire debris-flow volume emergency assessment model from Gartner et al. (2014). Gartner et al. (2014) measured 92 debris-flow volumes in the Transverse Ranges following storm events with a range of peak 15-min rainfall intensities, $i15$ (mm hr^{-1}), in recently burned (within past 2 years) catchments. They found that debris-flow volume, V (m^3), can be calculated as

$$\ln(V) = 4.22 + 0.39 \cdot \sqrt{i15} + 0.36 \cdot \ln(\text{Bmh}) + 0.13 \cdot \sqrt{R}, \quad (13)$$

where Bmh is the area of the catchment that burned at moderate to high severity (km^2), R is catchment relief (m), and \ln is the natural logarithm. We used this model along with measured morphologic characteristics of watersheds with different catchment-averaged erosion rates in the SGM to parameterize debris-flow volume as a function of uplift rate and drainage area, both of which are known for our model simulations.

To utilize Equation 13 to determine volume as a function of uplift rate and drainage area, we needed to cast relief, R , as a function of uplift rate and drainage area. To accomplish this, we used the mapped stream network, as elaborated in Section 3.1, for the 29 SGM catchments that we classified as being in an approximate steady state and that have also published ^{10}Be erosion rates (Figure 2; Table 1; DiBiase et al., 2010). For each node in the valley network upstream from an erosion rate sample site, we measured relief as the vertical distance from the channel node to the highest elevation within the area upstream. To ensure that our volume parameterization incorporates variability in uplift rate observed between catchments of varying size in the SGM, we plotted these relief values (units of meters) for each stream node as a function of upstream drainage area in each watershed (Figure S9 in Supporting Information S1). We found that for each catchment, the relationship between relief and drainage area is well-characterized by a power law ($R = f_1 A^{f_2}$; Figure S9 in Supporting Information S1; Table 1). In addition, the coefficients of these relief-drainage area relationships exhibit a power-law relationship with catchment averaged erosion rate ($f_1 = 2.20E^{0.29}$; Figure 4a; Table 1). These two relationships are intuitive as they indicate that catchment relief in steady-state landscapes is highest at large drainage areas and when uplift rate is fast. The exponent of the relief-drainage area power-law relationship exhibits no clear trend with uplift (Figure 4b; Table 1). We used these relationships to calculate R in Equation 13 for a given ^{10}Be erosion rate corresponding to each SGM catchment.

We used measurements of soil burn severity for recent fires in the SGM, including the 2016 Fish Fire and the 2016 Sand Fire, to estimate a reasonable value for the upstream area burned at moderate or high severity (Bmh) that could be used in Equation 13 (USDA Forest Service, 2022). Although burn severity can vary greatly within individual catchments and between catchments during a single fire, we found that an average value of $\sim 75\%$ of the watershed area burned at moderate to high severity (i.e., $\text{Bmh} = 0.75 \times A(x)$) is consistent with recent fires in the SGM.

Fifteen-minute rainfall intensity, $i15$, is necessary to calculate debris-flow volume with Equation 13. We used the post-wildfire debris-flow likelihood model from Staley et al. (2017) to estimate an $i15$ most appropriate for

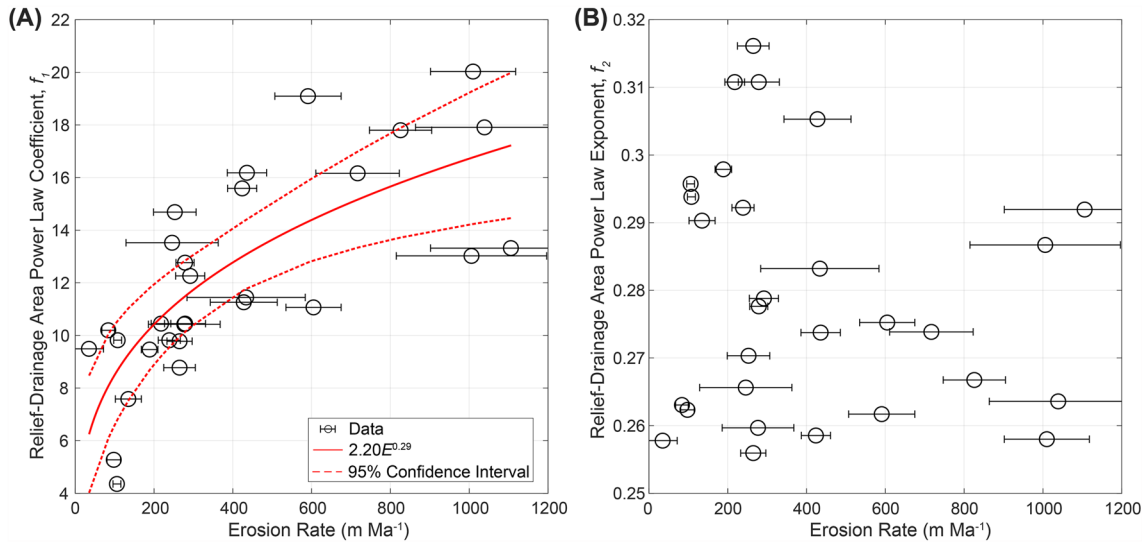


Figure 4. (a) The power-law coefficients for the relationship between relief and drainage area exhibit a power-law relationship with erosion rate. See Figure S9 in Supporting Information S1 for the power-law fits to relief-drainage area data for each catchment. Red line is the best-fit power law, and red dashed line is the 95% confidence interval. (b) The power-law exponents for the relief-drainage area relationship exhibit no significant relationship with erosion rate. In both panels, black circles represent the power-law coefficient or exponent for each catchment in the San Gabriel Mountains and error bars correspond to erosion rate uncertainty listed in Table 1.

triggering debris flows in the SGM. As laid out by Staley et al. (2017), the accumulated rainfall over a 15-min duration, R_A , necessary to trigger debris flows with probability, P , can be expressed as

$$R_A = \frac{\ln\left(\frac{P}{1-P}\right) - \beta_R}{C_1 T + C_2 F + C_3 S_E} \quad (14)$$

where $\beta_R = -3.63$, $C_1 = 0.41$, $C_2 = 0.67$, and $C_3 = 0.70$ are empirical parameters that dictate the relative roles of independent variables that determine whether a debris flow will occur. Specifically, T represents the proportion of upstream drainage area that burned at moderate or high severity and has slopes $\geq 23^\circ$, F is the differenced normalized burn ratio (dNBR) divided by 1,000 (i.e., dNBR/1,000), and S_E is the soil KF-Factor, or soil erodibility index. We estimated characteristic values of T (Figure S10 in Supporting Information S1), which varied weakly with uplift rate (Figure S11 in Supporting Information S1), as well as $F = 0.48$ (Table S2 in Supporting Information S1 shows dNBR values) and $S_E = 0.24$ based on the Sand and Fish Fires in the SGM (USDA Forest Service, 2022), and we determined the accumulated rainfall necessary for 50% likelihood that debris flows would be triggered ($P = 0.5$; Staley et al., 2017). We elaborate in more detail how we calculated T , F , and S_E in Supporting Information S1 (Text S2). We converted the calculated R_A to a characteristic i_{15} following

$$i_{15} = \frac{R_A}{D}, \quad (15)$$

where $D = 0.25$ hr represents the rainfall duration over 15 min. Taken together, we determined $i_{15} = 21$ mm hr $^{-1}$ and used this intensity to calculate debris-flow volume with Equation 13 (Figure 5). This value is consistent with previously calculated i_{15} for debris-flow initiation in the SGM (Staley et al., 2017) and has a recurrence interval <2 years, a value consistent with post-wildfire debris-flow initiation in the southwestern United States, including the SGM (Staley et al., 2020). We additionally utilized Equation 14 to determine whether debris-flow likelihood, and by extension frequency, varies with uplift rate or drainage area (through T). We found, however, that the observed relationships between T and uplift and drainage area were weak (Figures S10 and S11 in Supporting Information S1). Therefore, we assumed in our analysis that debris-flow frequency is not a function of uplift rate or drainage area.

3.3. Numerical Experiment Design

We ran a numerical experiment using the 1D landform evolution model described by Equation 3 to determine which values of α and β , the valley-bottom slope and flow-depth exponents, respectively, reproduced the

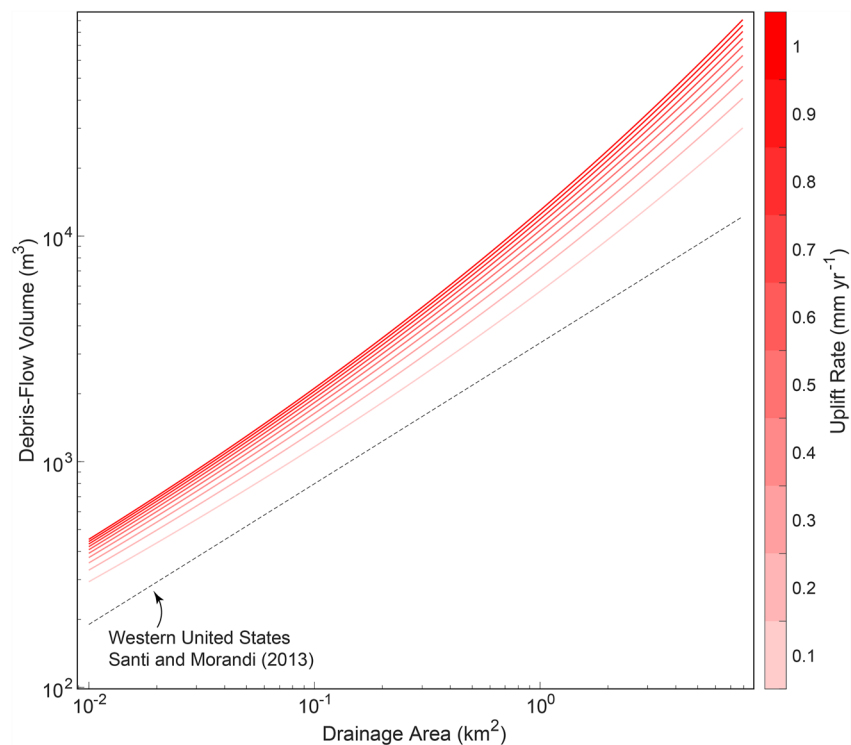


Figure 5. Debris-flow volume parameterized for the San Gabriel Mountains, following Equation 13, as a function of drainage area and uplift rate. Debris-flow volume is systematically larger than the predicted volumes for the western United States (dashed), as published by Santi and Morandi (2013) and expressed by $V = 3,357.5A^{0.7317}$, consistent with observations by Gartner et al. (2014).

relationships between uplift rate and A_{df} and S_0 in the SGM. In line with observations by McGuire et al. (2022), who noted that models using $\alpha < 3$ and $\beta > 2$ generally performed poorly but that $\alpha > 3$ and $\beta < 2$ produced naturally consistent valley profiles, we ran simulation sets with all combinations of α and β for $\alpha = 2, 3, 6$ and $\beta = 1, 2, 3$ to determine pairings that are capable of reproducing steep-land morphology of the SGM, as defined by relationships between E and A_{df} and S_0 (and a_1 in Supporting Information S1). Thus, exploring all α and β pairs results in a total of nine model sets (Table S3 in Supporting Information S1).

For each model set (i.e., one α, β pair), we ran simulations that systematically varied k_{df} and uplift rate. In a sensitivity test of model parameters, McGuire et al. (2022) observed that k_{df} , which accounts for factors such as grain size, bedrock erodibility, and debris-flow frequency, has a substantial effect on modeled longitudinal profiles, such that higher values of k_{df} (i.e., higher debris-flow efficiency, frequency) result in lower S_0 and higher A_{df} , all else equal. We tested a range of k_{df} in order to calibrate the parameter to the topography of the SGM. The relatively uniform lithology of the SGM makes a spatially constant k_{df} reasonable. As such, in this analysis k_{df} was varied but is a non-interpreted coefficient and not presented as results.

In summary, for each of the nine model sets, each with a distinct combination of α and β , we ran models with a range of k_{df} ($k_{df} = 1.0 \times 10^{-6} - 6.5 \times 10^{-5} \text{ m}^{1-\beta} \text{ s}^{-2}$; Table S4 in Supporting Information S1). For each value for k_{df} , we ran 10 simulations, each corresponding to a different uplift rate ($U = 0.1 - 1.0 \text{ mm yr}^{-1}$, increments of 0.1 mm yr^{-1}). This study design allowed us to isolate a single k_{df} that minimized the misfit between modeled catchment morphology as a function of uplift rate and that observed in the SGM. We elaborate on quantifying misfit between model results and the SGM below.

We kept values for debris-flow viscosity ($\mu = 1,500 \text{ Pa s}$) and yield strength ($\tau_y = 1,000 \text{ Pa}$) constant, as these parameters play little systematic role in setting morphology over the range of physically reasonable values and uplift rates (McGuire et al., 2022). Finally, to further limit the size of the parameter space and to consider debris-flow specific effects on valley-bottom form, we utilized a single value of K from the threshold-stochastic stream power incision model that, when paired with m_s and n_s values derived from the SGM (Text S1 in Supporting

Information S1; DiBiase & Whipple, 2011), produced consistent fluvial channel steepness values compared to previously observed values over a range of uplift rates in the SGM (Figure S12 in Supporting Information S1; DiBiase & Whipple, 2011). Models were run until valley profiles reached approximate steady state (<1 mm change in topography over 10 Kyr timestep), usually 10^6 – 10^7 yr.

3.4. Model Performance Assessment

We ran models using different pairs of α and β over a range of k_{df} and identified a single k_{df} for each α and β pairing that minimized the misfit between model results and the morphology of the SGM. Specifically, we quantified the misfit between model outputs across a range of uplift rates to bootstrapped fits to the SGM morphologic data for those same uplift rates as

$$\text{Misfit} = \sqrt{\frac{1}{N} \sum_1^N \frac{(\overline{Y_{boot}} - Y_{model})^2}{\sigma_{boot}^2}}, \quad (16)$$

where $\overline{Y_{boot}}$ is the mean of the bootstrap fits to a morphometric (A_{df} , S_0 , or a_1) for a particular uplift rate, Y_{model} is the model output morphometric for a given uplift rate, σ_{boot}^2 is the variance of bootstrap fits for a given uplift rate, and N is the number of model runs for each tested k_{df} ($N = 10$ for the 10 uplift rates used here). This misfit metric is a weighted least squares with σ_{boot}^2 varying as a function of uplift rate (Figure 3). The form of Equation 16 implies that at uplift rates where the morphometrics are well constrained (i.e., low σ_{boot}^2), the model is penalized more for not fitting the data than at uplift rates with higher σ_{boot}^2 . For a given k_{df} , lower values of this misfit metric correspond to better conformity between model output $A_{df} \sim E$ and $S_0 \sim E$ and that observed from the SGM as defined by the bootstrapped linear (A_{df}) and power-law (S_0) fits. Preliminary qualitative analysis of simulation results indicated that for some α , β pairs, morphometrics were constant as a function of uplift rate yet still exhibited low misfits. Therefore, we developed a technique to flag these model results, which we elaborate on in Supporting Information S1 (Text S3, Figures S13 and S14). In addition, although one might expect that the best-performing models for A_{df} and S_0 are found at the same values of α , β , and k_{df} , we found that this is not always the case. Hence, we explored fits based on misfits for A_{df} and S_0 individually as well as combined, which we elaborate below.

We used model flagging (Text S3 in Supporting Information S1) to identify α and β values that produced relationships between A_{df} and/or S_0 and erosion rate that were inconsistent with the SGM. For α and β pairs that were *not* flagged, we quantified misfit with Equation 16 to identify the best-performing α and β pairs for both A_{df} and S_0 in two ways. First, for a particular α , β pair across a range of tested k_{df} , we summed the misfits for $A_{df} \sim E$ and $S_0 \sim E$. We then identified the single k_{df} that exhibited the lowest *summed* misfit. We hereafter refer to this case as the *minimized summed misfit*. Because Equation 16 is independent of the magnitude of A_{df} or S_0 , summation does not bias toward one metric or the other. For this case of a minimized summed misfit, both A_{df} and S_0 produce sufficiently low misfits such that they *together* constitute modeled landscapes broadly consistent with the SGM across a range of uplift rates for a single k_{df} . Conceptually, these models capture (a) the slope of steepland valley headwaters (i.e., as quantified by S_0) and (b) the transition to the fluvial drainage network downstream (i.e., as quantified by A_{df}).

Calculation of the minimized summed misfit considers model performance for both A_{df} and S_0 , but a low value for the minimized summed misfit does not guarantee a low value for both components. We found that models that produced a low misfit for A_{df} did not always result in a low misfit for S_0 , and vice versa. Furthermore, the best performing models as defined by A_{df} may be optimized with one value of k_{df} , whereas the best performing model for S_0 may be optimized with a different value of k_{df} . Therefore, we also quantified the misfit for $A_{df} \sim E$ and $S_0 \sim E$ individually. That is, we tested a range of k_{df} for each α , β pair, and we identified the combination of α , β , and k_{df} that produced the most SGM-like landscapes as defined by *either* A_{df} or S_0 , without consideration for the performance of the other morphometric. We will refer to this as the *minimized individual misfit*. Conceptually, the minimized individual misfit corresponds to identifying the models that best reproduce *either* the (a) downstream extent of the debris-flow network in the SGM (i.e., as quantified by A_{df}) or (b) the distribution of SGM headwater slopes at low drainage areas (i.e., as quantified by S_0).

3.5. Debris-Flow Incision and Process Transitions

To test whether a spatial correspondence between the debris-flow to fluvial process transition and the morphometric signature A_{df} exists, we evaluated the relative location of A_{df} and the drainage area where $E_{df} = E_f$ for each

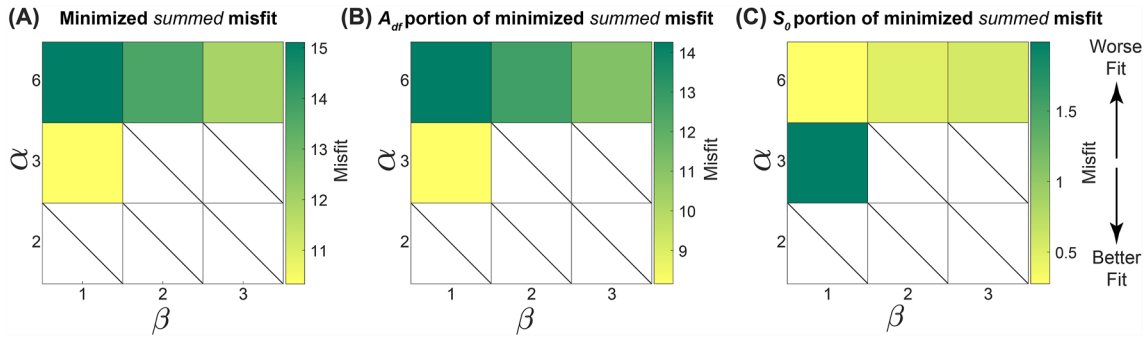


Figure 6. (a) The minimized summed misfit for model results compared to the San Gabriel Mountains (SGM) for different combinations of α and β . Yellow colors represent lower misfits, which highlight better fits to SGM morphologic data while green values correspond with higher misfits (see arrows on right). (b) Misfits for A_{df} that contribute to the summed misfit. (c) Misfits for S_0 that contribute to the summed misfit. In all three panels, white cells correspond with models that were flagged due to A_{df} values that are either invariant with uplift rate or exhibit a trend with uplift rate of the wrong sign (i.e., a negative relationship). No models were flagged for S_0 , but misfit was not minimized for S_0 for α, β pairs that were flagged for A_{df} (hence some S_0 cells are colored white). Note that for clarity of relative misfit values in each panel, the color axis scale differs between the three panels.

best-performing model as defined by the minimized summed misfit and minimized individual misfit. We refer to the location of equal debris-flow and fluvial incision as A_{50} . We compared calculated A_{50} for these models to A_{df} across the range of simulated uplift rates. We additionally calculated the proportion of total erosion at A_{df} that is accomplished by debris flows (i.e., $\frac{E_{df}}{E_f + E_{df}}$).

4. Results

4.1. San Gabriel Mountains Morphology

We observed that catchments in the SGM with faster erosion rates exhibit systematically larger A_{df} (Figures 2b and 3a), an observation consistent with that by Neely and DiBiase (2023) that also reflects the lengthening of steep headwater, debris-flow valleys noted by DiBiase et al. (2012). Specifically, the relationship between erosion rate and A_{df} is approximately linear ($A_{df} = 0.37E + 0.08$; Figure 3a; Table 1), such that faster-eroding catchments have steeper valleys that extend farther downstream. We correspondingly observed that the relationship between erosion rate and a_1 approximates an inverse power law ($a_1 = 2.07E^{-0.28}$; Figure S7 in Supporting Information S1; Table 1). Furthermore, we noted that S_0 is not constant through the entire range of erosion rates in the SGM. Rather, S_0 is lowest in slowly eroding catchments and increases with erosion rate, approximating a power-law relationship ($S_0 = 0.7E^{0.15}$; Figure 3b; Table 1). However, at erosion rates $> \sim 0.4 \text{ mm yr}^{-1}$, S_0 may approach a constant value (Figure 3b).

4.2. Landform Evolution Model

We used the 1D landform evolution model to test all combinations of $\alpha = 2, 3, 6$ and $\beta = 1, 2, 3$, and we calibrated k_{df} for each α, β pair by identifying the single k_{df} that minimizes misfit (Equation 16) between modeled valley longitudinal profiles and those in the SGM. We observed that across simulated uplift rates of $0.1\text{--}1.0 \text{ mm yr}^{-1}$, A_{df} and S_0 visually exhibited varying degrees of overlap with the same metrics derived in the SGM (Figures 7 and 9; Figures S16 and S18 in Supporting Information S1 for a_1), which were also reflected by the quantified misfits (Figures 6 and 8; Figures S15 and S17 in Supporting Information S1 for a_1). Similar to McGuire et al. (2022), we found that larger values of α generally produced more reasonable valley profiles that are consistent with the SGM. We additionally observed that for $\alpha = 3, \beta > 1$ and all models where $\alpha = 2$ produced flagged results (Figures 6 and 8, Figures S16 and S18 in Supporting Information S1), as A_{df} for these α, β pairs was either invariant with uplift rate or exhibited lower values at fast erosion rates, which is the opposite from that observed in the SGM.

4.2.1. Model Performance of a_1 and S_0 : Minimized Summed Misfit

The best-performing model, as defined by the *minimized summed misfit*, corresponded to exponents $\alpha = 3$ and $\beta = 1$, although models where $\alpha = 6$ produced unflagged results for all tested β (Figure 6). In general, model misfit was less sensitive to β than to α . Although we observed that $\alpha = 3, \beta = 1$ was the best exponent pairing

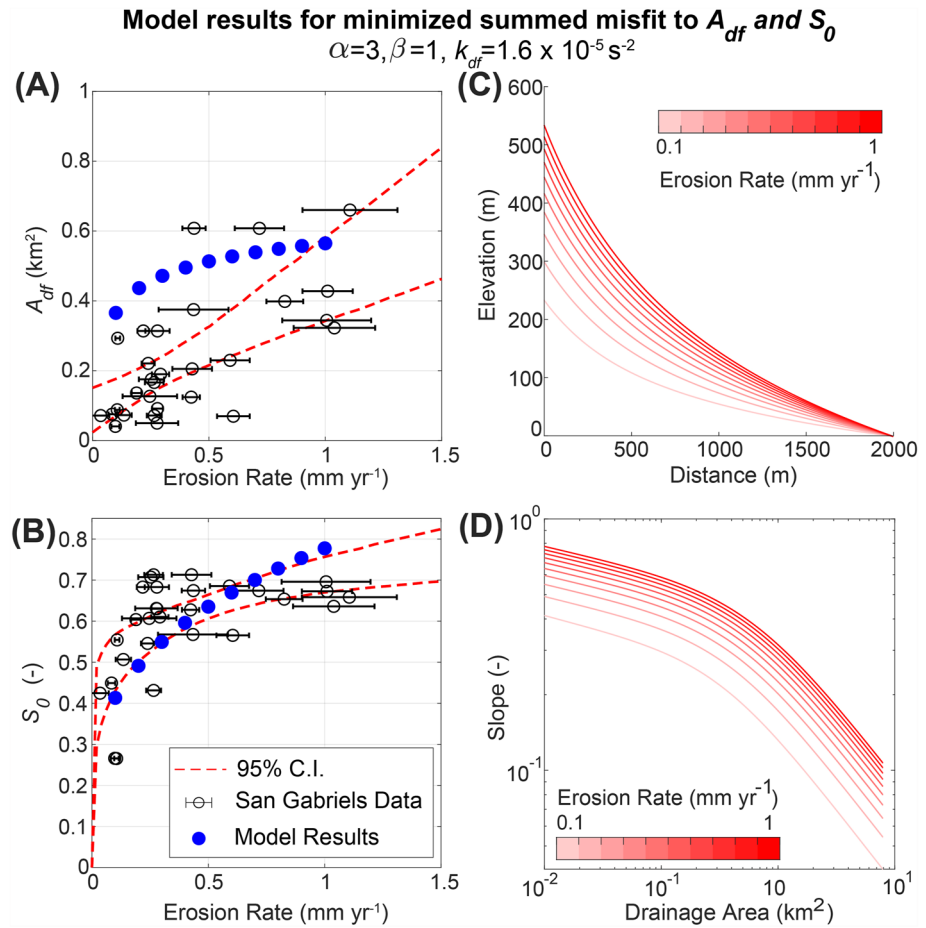


Figure 7. (a, b) Model results (blue dots) for the *overall* best-performing model ($\alpha = 3, \beta = 1$ in Figure 6) compared to the morphologic data from San Gabriel Mountains (black circles with error bars). Results for A_{df} are shown in (a) and S_0 is shown in (b). Note that while this is the best-performing model *overall*, as defined by both A_{df} and S_0 , it is not the best performing models for A_{df} and S_0 individually, which is most apparent for A_{df} in (a), as the model results fall outside the 95% confidence intervals (red dashed). Steady-state longitudinal profiles (c) and slope-area plots (d) for valleys corresponding to model runs in (a) and (b). Valleys and slope-area data are colored by model-defined uplift rate. See Figure 9 for the best-performing models for A_{df} and S_0 as defined by the minimized individual misfit. Units for k_{df} are $\text{m}^{1-\beta} \cdot \text{s}^{-2}$ ($\beta = 1$ for all models shown here).

when considering the summed misfits for A_{df} and S_0 , we additionally evaluated this summed misfit separated into its A_{df} and S_0 components. Note, this is not the same thing as the minimized individual misfit, which we discuss in the next section. Rather, this is simply the two misfits for A_{df} and S_0 , which, when summed, constitute the minimized summed misfit. In this case, we observed that the best performing α, β pair corresponded to $\alpha = 3, \beta = 1$ for A_{df} (Figure 6b). However, although $\alpha = 3, \beta = 1$ reasonably reproduced the observed $A_{df} \sim E$ relationship, it was one of the poorer performing pairs when it comes to reproducing the observed $S_0 \sim E$ relationship, which exhibited misfits > 0.27 (Figure 6c); the best parameter pair for S_0 was $\alpha = 6, \beta = 1$ (Figure 6c), although A_{df} produced a misfit > 14.2 (Figure 6b). Put another way, identifying a single α and β pair for both A_{df} and S_0 means that sacrifices to model performance may be necessary by A_{df} or S_0 to ensure an *overall* good fit. Thus, although $\alpha = 3, \beta = 1$ was the best performing model *overall*, it did not ideally reproduce SGM morphology as defined separately by A_{df} and S_0 (Figures 6b and 6c). This was particularly true for A_{df} (Figure 7a). We observed similar results for modeled a_1 values (Figures S15 and S16 in Supporting Information S1).

4.2.2. Model Performance of a_1 and S_0 : Individual Misfit

Whereas the previous section considers the α, β pairs that produced the best fit to the SGM as defined by both A_{df} and S_0 , here we consider the α and β pairs that produced the best fit between A_{df} or S_0 and erosion in the SGM *individually* (Figures 8 and 9). Here, we minimized misfit for A_{df} and S_0 separately. Thus, for a single α, β pair,

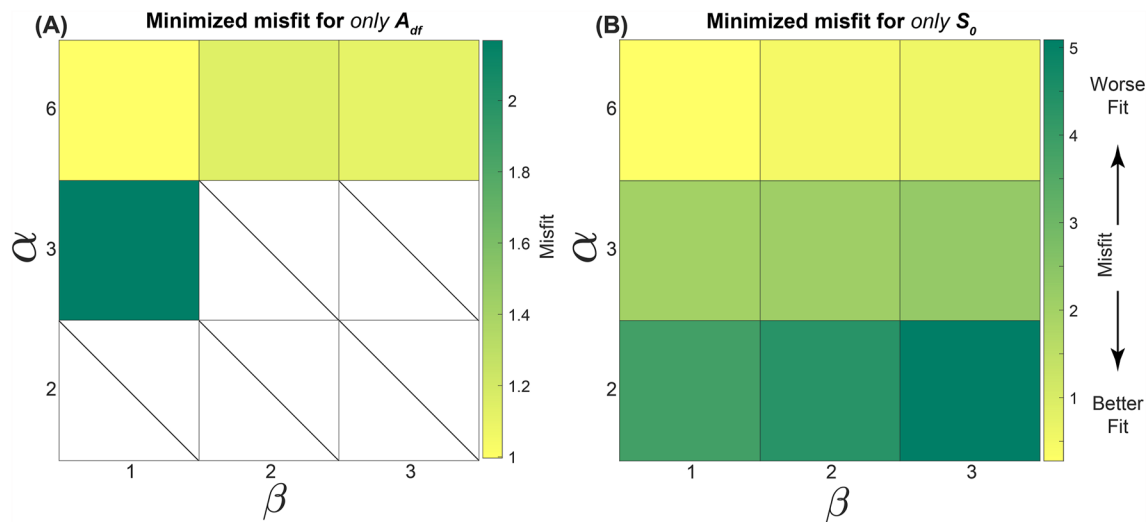


Figure 8. The minimized misfit for A_{df} (a) and S_0 (b) when considered individually for model results compared to the San Gabriel Mountains (SGM). (a) The best-performing model when only considering A_{df} corresponds to $\alpha = 6, \beta = 1$, where misfit is ~ 1 . (b) The best-performing model runs when only considering S_0 correspond with $\alpha = 6, \beta = 1$, although all models with $\alpha = 6$ have misfits < 0.6 . In both panels, yellow colors correspond with lower misfit values and better conformity with the SGM, while green colors correspond with worse fits (see arrows on right). In (a), colorless cells correspond with flagged models where A_{df} exhibits an invariant or incorrect-sign trend with uplift rate. Note that model runs between (a) and (b) likely do not correspond to the same k_{df} (i.e., they come from different individual model runs; Table S4 in Supporting Information S1). Note that the color axis scale differs between the two panels.

the model for which A_{df} misfit was minimized does not necessarily utilize the same k_{df} as S_0 (i.e., they are separate model runs; Table S4 in Supporting Information S1).

We found that the best performing models occurred at similar α, β pairs to minimized summed misfit for A_{df} and S_0 . For both A_{df} and S_0 , we observed that misfit was lowest for $\alpha = 6, \beta = 1$, although model misfit was low for all α and β that were not flagged, corresponding to $\alpha = 6$ and all tested β (all misfits < 1 for S_0 and < 1.2 for A_{df} ; Figure 8a), especially compared to the values reported for the minimized summed misfit in the previous section (all misfits > 10 ; Figures 6a and 6c). Misfit for S_0 was highest ($> \sim 2$) for $\alpha \leq 3$ (Figure 8b).

4.3. Debris-Flow Incision

For the model runs where we minimized misfit between model results and the SGM, we additionally identified the drainage area at which incision by debris flows is equal to fluvial incision (A_{50}). We observed that across uplift and erosion rates from 0.1 to 1.0 mm yr⁻¹ and for all metrics for which we minimized misfit to the SGM, the drainage area at which fluvial incision began to outpace debris-flow incision was conspicuously smaller than A_{df} . For example, for the case of misfit minimized for A_{df} and for erosion rates of 0.1 and 1.0 mm yr⁻¹, A_{df} occurs at 0.14 and 0.35 km², respectively, whereas A_{50} is located at 0.03 and 0.1 km², respectively (Figures 10a and 10d, Figure S19b in Supporting Information S1). Similarly, for models with misfit minimized for S_0 and erosion rates of 0.1 and 1.0 mm yr⁻¹, A_{df} occurs at 0.4 and 1.1 km², while A_{50} is located at 0.1 and 0.36 km², respectively (Figures 10a and 10e, Figure S19c in Supporting Information S1). For each of these cases, $A_{df} > A_{50}$, and as uplift and erosion rate increase, the difference between A_{50} and A_{df} increases. In contrast, Figures 10a and 10c show that for an erosion rate of 0.1 mm yr⁻¹ when the summed misfit is minimized ($\alpha = 3, \beta = 1$), $A_{df} = 0.37$ km² but $A_{50} = 0.26$ km², whereas for an erosion rate of 1.0 mm yr⁻¹, both A_{df} and A_{50} are ~ 0.56 km² (Figures 10a and 10c, Figure S19a in Supporting Information S1). Hence, in this case, $A_{df} > A_{50}$ at slow erosion rate, but A_{50} converges with A_{df} at faster erosion rates.

In addition, we measured the proportion of total erosion at A_{df} that was accomplished by debris flows (i.e., $\frac{E_{df}}{E_f + E_{df}}$). We observed that for all tested uplift and erosion rates, debris-flow erosion generally only accounts for a small proportion of the total erosion at A_{df} , and this proportion varies with erosion rate. Specifically, Figure 10b shows that for the case of the minimized individual misfit for A_{df} , debris flows account for 2% and 4.1% of total erosion at A_{df} for erosion rates of 0.1 and 1 mm yr⁻¹, respectively. Similarly, for the case of minimized individual misfit for S_0 , only 3.7% and 7% of total erosion at A_{df} is accomplished by debris flows for erosion rates of 0.1 and

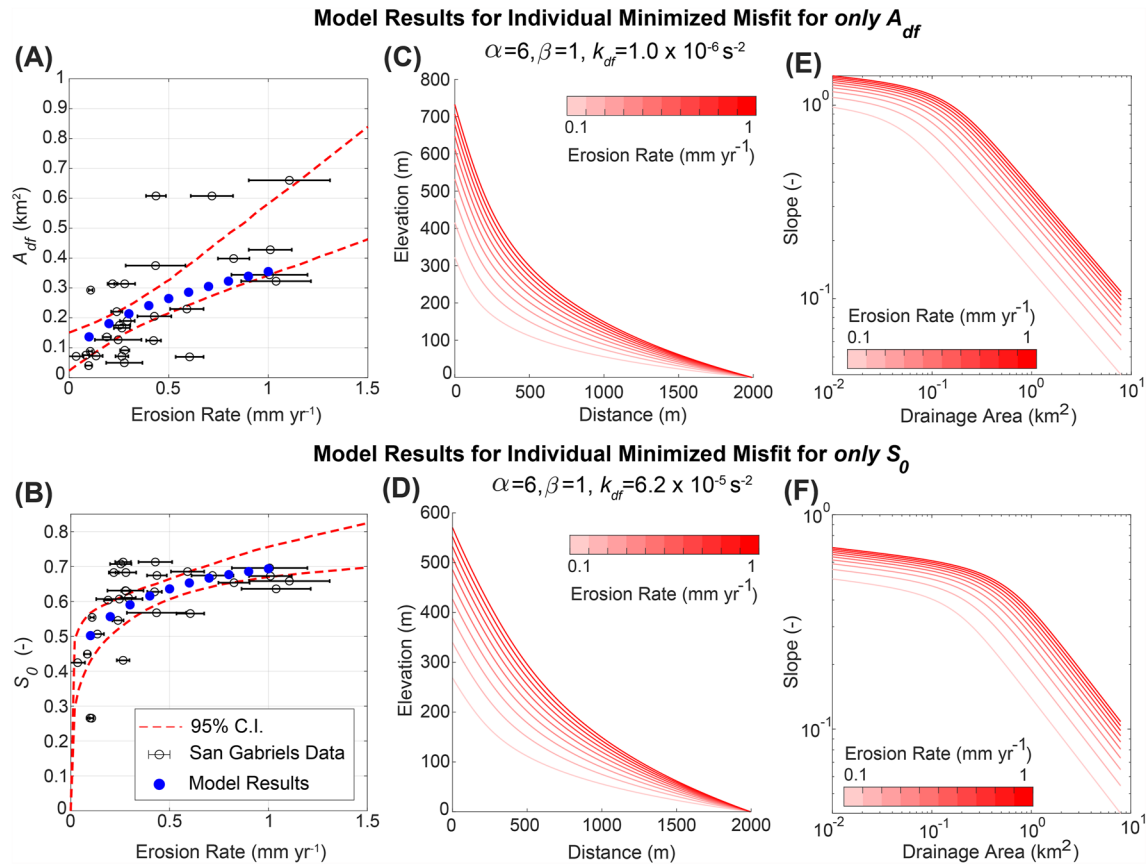


Figure 9. (a, b) Model results (blue dots) for (a) the best performing model for A_{df} without regard for S_0 performance (see $\alpha = 6, \beta = 1$ in Figure 8a), and results for (b) the best-performing model for S_0 , without regard for A_{df} performance (see $\alpha = 6, \beta = 1$ in Figure 8b). Gray circles with error bars are catchment data for the San Gabriel Mountains. Red dashed lines are 95% confidence intervals to bootstrapped power-law fits. Steady state longitudinal profiles (c, d) and slope-area plots (e, f) for valleys corresponding to model runs in (a) and (b). Channels and slope-area plots are colored by model-defined uplift rate. Units for k_{df} are $m^{1-\beta} \cdot s^{-2}$ ($\beta = 1$ for all models shown here).

1 mm yr⁻¹, respectively (Figure 10b). Finally, for the case of the minimized summed misfit, debris-flow erosion accounts for a comparatively high 39% and 50% of total erosion at A_{df} for erosion rates of 0.1 and 1 mm yr⁻¹, respectively (Figure 10b). Importantly, the higher proportion of erosion completed by debris flows at A_{df} for the model where we minimized the summed misfit corresponds to a lower α ($\alpha = 3$) than for the models where we minimized misfit individually for A_{df} and S_0 ($\alpha = 6$) and exhibits a greater misfit than for the misfit minimized for only A_{df} .

5. Discussion

5.1. Inferring Climate and Tectonics: Debris-Flow Network Morphology

Our morphologic analysis of the SGM builds upon the work of Stock and Dietrich (2003) and Penserini et al. (2017) in the Oregon Coast Range and demonstrates that steep-land network structure, as defined by the curvature of slope-area plots, approximates landscape-scale uplift and erosion rates. These results reflect observations by DiBiase et al. (2012) and Neely and DiBiase (2023), who noted a denser steep-land drainage network with longer channels, including as quantified by A_{df} , in catchments with fast erosion rates. For the case of a_1 , the relationship we observed between erosion rate and a_1 differs from that in the Oregon Coast Range by Penserini et al. (2017; dashed line in Figure S20a of the Supporting Information S1). While the magnitudes of erosion rate and a_1 differ between these two landscapes, the differing power-law relationships between erosion rate and a_1 in the SGM and Oregon Coast Range may be due to contrasts in lithology and grain size in steep catchments. Indeed, Neely and DiBiase (2023) noted that A_{df} and S_0 exhibit positive correlations with median bed sediment

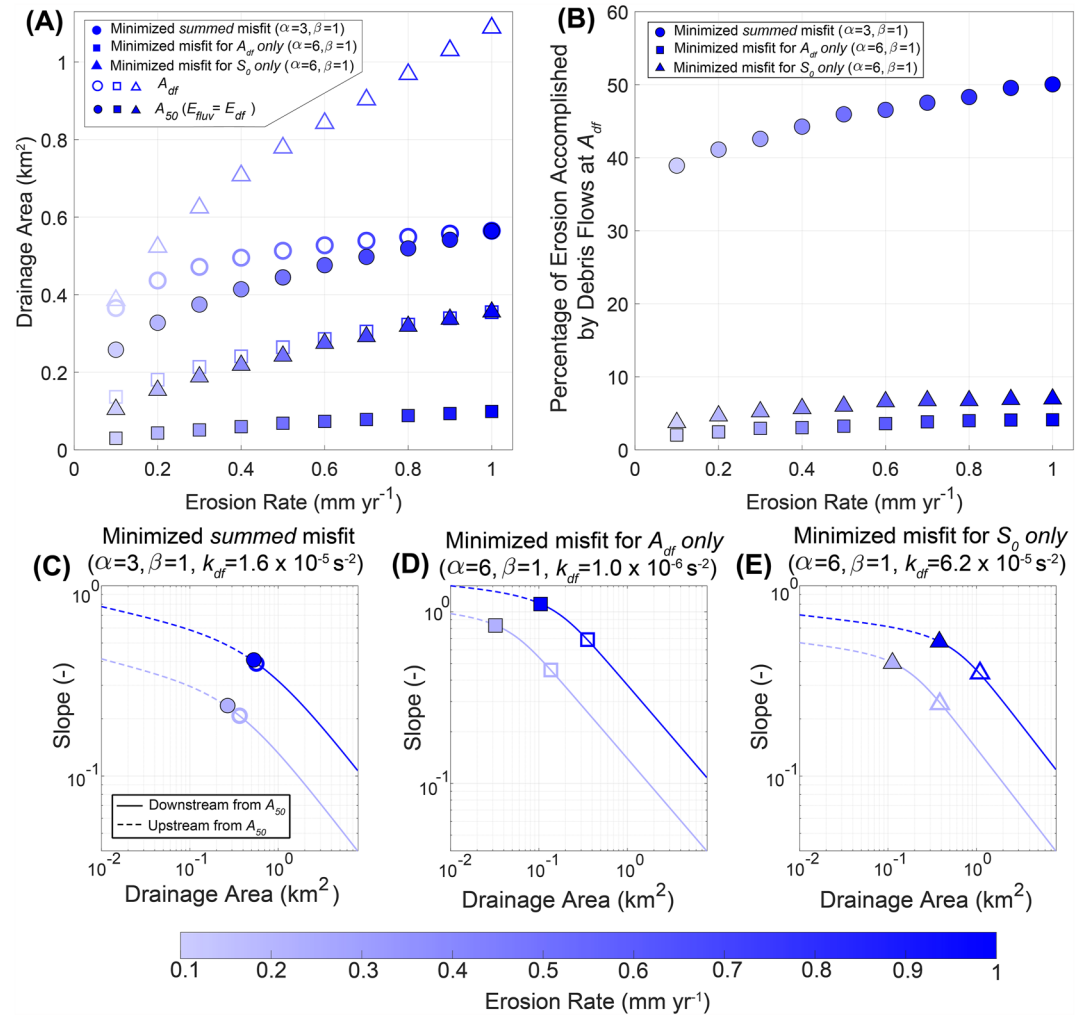


Figure 10. (a) The drainage area at which A_{df} occurs (open symbols) compared to the drainage area where fluvial and debris-flow incision are equal, A_{50} (filled, colored by erosion rate). Circles correspond to models for the minimized summed misfit ($\alpha = 3, \beta = 1$), squares are models where the misfit was minimized only for A_{df} ($\alpha = 6, \beta = 1$; different k_{df} from minimized summed misfit), and triangles are models where misfit was minimized for only S_0 ($\alpha = 6, \beta = 1$). Note that A_{df} occurs at drainage areas larger than those where the process transition (A_{50}) occurs, regardless of the α and β values used, although A_{df} and A_{50} converge at more rapid erosion rates for $\alpha = 3, \beta = 1$ in (a). For the two model sets with $\alpha = 6, \beta = 1$, this difference between A_{df} and A_{50} is largest at fast erosion rates. (b) The proportion of incision at A_{df} that is accommodated by debris flows. Note that debris-flow incision is significantly less than fluvial incision, except for $\alpha = 3, \beta = 1$ where debris-flow incision is only slightly less than fluvial incision. Symbology is the same as in (a). (c–e) Slope-area plots for $E = 0.1 \text{ mm yr}^{-1}$ (light blue) and $E = 1 \text{ mm yr}^{-1}$ (dark blue) for the minimized summed misfit (c), minimized misfit for A_{df} (d), and minimized misfit for S_0 (e). Dashed and solid lines correspond to the portions of the profiles up- and downstream from A_{50} (filled), respectively, while dotted vertical lines demarcate the drainage area at which A_{df} (open symbols) occurs. The drainage area at which the dashed and solid portions of the slope-area plots meet corresponds to the A_{50} plotted in (a). Symbology of (c–e) is the same as in panel (a). Units for k_{df} are $\text{m}^{1-\beta} \cdot \text{s}^{-2}$ ($\beta = 1$ for all models shown here).

size, indicating that the ability of fluvial and debris-flow processes to entrain sediment helps set the location of A_{df} . In addition, variable relationships between erosion rate and A_{df} (or a_1) between the SGM and Oregon Coast Range may also be due to differences in debris-flow recurrence interval and debris-flow volume-drainage area scaling and how these properties may or may not systematically vary as a function of uplift rate. McGuire et al. (2022) observed that systematic relationships between k_{df} and uplift rate as well as debris-flow volume (i.e., through scaling exponent γ) and uplift rate result in notable changes to modeled trends between uplift rate and steepland morphology. For example, although Penserini et al. (2017) did not observe a clear relationship between erosion rate and S_0 in the Oregon Coast Range, discerning whether this is due to a lack of uplift control on debris-flow valley headwater steepness or rather a systematic variation of debris-flow frequency or volume with uplift

rate is challenging. In the SGM, we observed no clear indication of systematic variation of debris-flow frequency with uplift rate when applying the post-wildfire debris-flow likelihood model of Staley et al. (2017) (Figure S11 in Supporting Information S1; Equation 14), although we noted that the lowest erosion-rate catchments may exhibit a clearer relationship between uplift rate and debris-flow likelihood. Furthermore, our parameterization of debris-flow volume considers explicit variation of flow volume with uplift rate that is apparent from the model of Gartner et al. (2014). Thus, we emphasize the ideal nature of the SGM as a natural laboratory for investigating how debris flows set steepland form, due to the abundance of debris-flow data that have been collected over the past several decades. In other landscapes, including the Oregon Coast Range, future studies on A_{df} and S_0 (and a_1) would benefit from additional interrogation of debris-flow volume and frequency relationships with uplift rate.

The power of A_{df} (as well as S_0 and a_1) to predict erosion rate places it amongst other landscape morphometric quantities to interpret landscape-scale climate and tectonics. Specifically, metrics derived from the fluvial drainage network, such as channel steepness, have exhibited success in many landscapes in interpreting regional uplift rates, identifying active faults and isolating recent changes to the spatial extent of drainage networks (Hurst et al., 2019; Kirby & Whipple, 2012; Willett et al., 2014). Similarly, hilltop curvature has been demonstrated as a predictor of erosion rate in soil-mantled landscapes (e.g., Hurst et al., 2012; Roering et al., 2007). However, fluvial metrics lose their predictive power in steeplands, as channels reach a threshold steepness and debris flows dominate incisional processes at low drainage areas (Hilley et al., 2019; Stock & Dietrich, 2003), and hilltop curvature becomes an ineffective estimate of erosion rate in steep, rapidly eroding landscapes where soils become patchy and hilltops become conspicuously narrow and sharp (Gabet et al., 2021; Heimsath et al., 2012; Neely et al., 2019; Struble & Roering, 2021). As such, A_{df} , S_0 , and a_1 present an exciting framework for estimating relative uplift and erosion rates between catchments in landscapes where fluvial and hillslope metrics become ineffective. However, the predictive application of A_{df} , S_0 , and/or a_1 is limited by the largely empirical nature of the relationship between these metrics and erosion rate, and more theoretical work would be beneficial to explicitly link steepland morphology with climate and tectonics within an analytical framework (McGuire et al., 2022). Nevertheless, in individual landscapes, cross-divide differences in A_{df} or a_1 (and S_0) between neighboring catchments provide an estimate of relative erosion rates.

Although relationships between erosion rate and form in steepland catchments have typically relied on A_{df} and a_1 , we observed that S_0 systematically varies with erosion rate in the SGM as well, in contrast to previous suggestions that steepland valley-bottom slope is invariant with uplift rate and is primarily set by material properties or is an extension of threshold hillslopes (e.g., Penserini et al., 2017). We note, however, that valley bottoms, including in our model framework where hillslope processes are absent, may reach a threshold slope, akin to threshold hillslopes that become insensitive to further increases in erosion rate (Larsen & Montgomery, 2012; Montgomery, 2001; Roering et al., 1999; Figures 3b, 7b, and 9b). Rather than an angle of repose set by granular and geotechnical properties of soil, S_0 is set by systematic variation between uplift and k_{df} and scaling relationships between debris-flow volume and drainage area (McGuire et al., 2022). In addition, the rate at which S_0 scales with uplift rate is set by the slope exponent, α (Figures 6 and 8; McGuire et al., 2022).

5.2. Constraining a GTL for Debris-Flow Incision

The scatter we observed in the morphologic data for the SGM introduced challenges for identifying model parameters, notably α , β , and k_{df} , that produced best-fit results to the SGM. Although we were able to capture the variability in SGM morphology utilizing bootstrapping, model misfits for A_{df} and S_0 demonstrated that although some α and β pairs produced clearly unreasonable results that did not conform to the SGM or most natural landscapes (i.e., $\alpha = 2$ for all β , $\alpha = 3$ for $\beta > 1$), no single α and β pair produced clearly superior results compared to other pairs. Some α , β pairs produced modeled valley profiles that were highly consistent with the SGM for one morphometric (e.g., A_{df}) but not for the other. This was further highlighted by the fact that the pairing of $\alpha = 3$, $\beta = 1$, which minimizes the summed misfit, yields a misfit that is quite high (>10) relative to what it could be when considering each morphometric individually (Figures 8b and 8c). We hypothesize that the inability of the model to reproduce the observed relationships between erosion rate, A_{df} , and S_0 with fixed α , β , and k_{df} is due, in part, to uncertainties in (a) debris-flow volume, particularly at small drainage areas, (b) debris-flow likelihood as a function of uplift rate due to variations in sediment supply, and (c) valley-bottom width in debris-flow-dominated reaches. We discuss each of these three topics below in Section 5.3. Other parameters that we assume constant in our models, notably K , m_s , and n_s , may systematically vary with uplift rate and affect our ability to accurately fit

both A_{df} and S_0 to the SGM. Nevertheless, our observation that, in general, higher α and lower β produce modeled landforms that are consistent with natural examples reflects observations by McGuire et al. (2022).

The ambiguity of ideal slope and depth exponents is consistent with remaining open questions for other GTLs. For example, numerous works have explored appropriate values for exponents corresponding to drainage area, m , and slope, n , in the stream power incision model and what properties, such as lithology, climate, and sediment supply may be encapsulated by these parameters (e.g., Clubb et al., 2016; Lague, 2014; Schwanghart & Scherler, 2020; Turowski, 2021; Whipple & Tucker, 1999). Indeed, one would be hard-pressed to find single values of m and n that can be applied universally. In a similar fashion, even though we cannot identify single α or β values that can be applied universally, our results indicate that higher and lower values of α and β , respectively, tend to produce more physically reasonable landscapes, which reinforces the strong nonlinear dependency of valley-bottom slope on debris-flow incision. Nevertheless, these results may encourage future work, particularly experimental and field studies, to examine the slope- and depth-dependency of debris-flow incision rate. In addition, the utilization of a 2D modeling approach may more clearly incorporate drainage network and topological effects into debris-flow impacts on resulting morphology and the reasonable range of parameters that produce modeled landforms consistent with natural examples.

5.3. Model Limitations and Opportunities for Future Work

5.3.1. Volume Model

We parameterized debris-flow volume for the SGM using the empirical emergency assessment model from Gartner et al. (2014). However, whereas this model is designed to capture variability in debris-flow volumes *between* catchments, we additionally apply this model to estimate variation in debris-flow volume *within* catchments as a function of drainage area. As such, our calculation of debris-flow volume may not fully capture the details of the drainage area dependence of debris-flow volume in the SGM, particularly at low drainage areas. For example, Rengers et al. (2021) measured sediment volumes exported from watersheds following the 2016 Fish Fire in the SGM. Their observed volumes are in close agreement with the debris-flow volumes predicted by Gartner et al. (2014) at large drainage areas ($>0.1 \text{ km}^2$), whereas at small drainage areas they noted sediment yield volumes less than those predicted by the Gartner et al. (2014) empirical model, often by nearly a factor of 5. Although Rengers et al. (2021) do not explicitly measure the volumes of debris flows but of sediment yield more generally, their observations highlight the importance of future observations of debris-flow volume variability *within* individual catchments, in addition to comparisons between catchments. Improved representation of debris-flow volume, particularly at smaller drainage areas, may help reduce error in the relationship between modeled S_0 and erosion rate.

Due to the remaining open questions regarding debris-flow volume as a function of drainage area, application of the landform evolution model we use here to other landscapes would ideally consider landscape-specific relationships between debris-flow volume and drainage area (Gartner et al., 2008; Wall et al., 2022) and would not rely on the debris-flow parameterization that we use for the SGM. Indeed, the ability to parameterize debris-flow volume, and its relation to local uplift rate, within a debris-flow GTL is a substantial challenge for constraining debris-flow effects on landscape form within a particular landscape.

5.3.2. Sediment Supply

The 1D landform evolution model we utilize here considers debris-flow incision as a function of debris-flow volume (through depth term, h , in Equation 6), which is parameterized as a function of drainage area and uplift rate. However, in this initial application of the model in a natural landscape, we do not consider variations in debris-flow volume due to time since the last debris flow or limits in sediment supply to valleys due to fire recurrence intervals (e.g., DiBiase & Lamb, 2020; Lamb et al., 2011). In natural landscapes, debris-flow initiation and incision is limited by the quantity of sediment supplied to valley bottoms, and in the SGM, hillslope-channel sediment coupling is driven largely by post-wildfire processes including dry ravel (DiBiase & Lamb, 2020). In addition, assuming steady state, sediment supply and grain size from the hillslopes to the debris-flow network will vary as a function of uplift, particularly over long timescales (Heimsath et al., 2001, 2012; Larsen & Montgomery, 2012; Neely & DiBiase, 2020, 2023; Neely et al., 2019; Reneau & Dietrich, 1991). Specifically, channels experiencing slow uplift rates are likely to have decreased hillslope-derived sediment as the availability of bedrock at the surface for weathering and eventual transport occurs more slowly and soil accumulates (Almond

et al., 2007; Heimsath et al., 2001; Sweeney et al., 2012; Townsend et al., 2021). In a similar fashion, catchments with fast uplift rates will have enhanced sediment supply; thus, debris-flow incision will be less inhibited by the availability of sediment in valley bottoms, but rather by the debris-flow recurrence interval (DiBiase & Lamb, 2020; Lamb et al., 2011). The transport capacity of debris flows and water-dominated flows will be modulated by the size of sediment supplied to the drainage network, which may additionally affect debris-flow recurrence as well as the location of morphologic and process transitions (Lai et al., 2021; Neely & DiBiase, 2023). We did not explicitly consider these constraints in our model. Currently, debris-flow frequency and erodibility (including grain size and sediment supply) are encapsulated within k_{df} . However, future studies could explore a parameterization for debris-flow likelihood that includes interactions among erosion rate and sediment supply. This would introduce additional parameters but may be necessary for improving the model's ability to simultaneously match trends between erosion rate, S_0 , and A_{df} .

5.3.3. Valley Width

We utilized empirical relationships between channel width and drainage area observed in the SGM by DiBiase and Whipple (2011) as expressed in Equation 5. However, these measurements were spatially limited in scope to the fluvial drainage network. Although field observations have noted that channels and steepland valley bottoms affected by debris flows tend to be wider than fluvial bedrock channels (Kean et al., 2016; May et al., 2013; Montgomery & Gran, 2001; Neely & DiBiase, 2023), it remains unclear what scaling relationships may exist between channel or valley-bottom width and drainage area in steep valleys frequently traversed by debris flows, how this scaling relationship may vary as a function of uplift and climate, rock type, and vegetation, amongst other properties, and how it transitions to width-area scaling relationships in the fluvial drainage network. Importantly, systematic changes in the width of valley bottoms at low drainage areas may affect the extent to which deviations of power-law slope-area scaling at low drainage areas can be uniquely connected with debris-flow incision. For example, reductions in valley-bottom width at low drainage areas relative to what is expected from width-area scaling relationships derived from higher-order fluvial channels could result in lower-than-anticipated valley-bottom slopes.

Future work, therefore, could extend existing channel width-drainage area scaling relationships to low drainage areas, spanning a range of uplift rates, akin to ongoing efforts for fluvial drainage networks (e.g., May et al., 2013; Schanz & Montgomery, 2016; Tomkin et al., 2003; Yanites, 2018). From the perspective of debris-flow incision, high confinement of debris flows due to narrow channels implied by the width-area scaling from DiBiase and Whipple (2011) can produce debris flows with high velocities and flow depths, particularly if debris-flow volume is poorly parameterized. Although our model results emphasize the importance of channel slope over debris-flow depth (Figures 6 and 7; McGuire et al., 2022), variations in calculated debris-flow depth may affect incision by debris flows such that resulting channel slopes adjust accordingly, thus perhaps changing the ideal values of α and β that reproduce the morphology of natural, steep landscapes. However, initial model sensitivity tests revealed that increasing the valley-bottom width by adjusting the coefficient in width-area scaling for debris-flow incision, as quantified by Equation 6, results in changes in the relationships between A_{df} and S_0 and erosion rate that can be absorbed by variations in k_{df} . As such, although our model results do not reveal a single k_{df} or α , β pair that perfectly reproduce relationships between erosion rate and A_{df} and S_0 (Figures 6 and 7), changes to valley-bottom width at low drainage areas do not alone improve this outcome.

5.3.4. Valley Heads and Network Structure

The landform evolution model we utilize here is 1D. However, incorporating the proposed debris-flow GTL into a 2D landscape evolution model has clear advantages. For example, Stock and Dietrich (2003) found that the number of upstream debris-flow sources, which they termed "trigger hollows," scales with debris-flow erosion. They found that accurately capturing the number of upstream debris-flow sources as a function of drainage area is crucial for reproducing reasonable steepland landscapes as well as the "stepped" longitudinal profiles that they observed at valley confluences (Stock & Dietrich, 2003). Put another way, debris-frequency varies in a landscape not only due to a characteristic recurrence of processes responsible for triggering debris flows (e.g., fire, rainfall) but also with position in a valley network. As such, a 2D landscape evolution model would allow for explicit representation of the stochastic triggering of debris flows at "trigger hollows," particularly for landscapes that experience landslide-initiated debris flows (Stock & Dietrich, 2003). In landscapes such as the SGM where debris flows initiate as runoff rapidly entrains sediment from spatially distributed source areas throughout a drainage basin (Staley et al., 2014), a 2D landscape evolution model will permit explicit consideration of

relationships between upslope terrain attributes, debris-flow likelihood (Staley et al., 2017), and debris-flow volume (Gartner et al., 2014). Similarly, how often variably mobile debris flows traverse discrete portions of the drainage network will affect spatially variable debris-flow frequency throughout the steep-land valley network (Shelef & Hilley, 2016). In our current erosion law, k_{df} subsumes the effects of debris-flow frequency, but future 1D or 2D models could utilize spatially variable k_{df} to capture topologic effects on frequency, which would be non-trivial given the finite runout distance of debris flows.

Beyond the 2D network structure, this paper specifically focused on A_{df} as the morphologic transition point from steep-land valley bottoms to fluvial channels but neglects potential variations in the transition from hillslopes to debris-flow dominated valley bottoms. We have only modeled the steep-land valley network downstream from the transition from hillslopes to debris-flow dominated valley bottoms. Including hillslope processes would allow for simultaneous exploration of the hillslope-to-steep-land-valley transition and the steep-land-valley-to-fluvial transition as well as more explicit constraints on the sediment supply available to initiate debris flows at valley heads. Such model investigations would be aided by topographic analysis of actual landscapes to objectively map the upper-most extent of steep-land valley bottoms (i.e., “valley heads”) at the base of hillslopes, as has been done for fluvial channels (e.g., Clubb et al., 2014), as well as by quantifying how this location may systematically vary with uplift rate. These model efforts would additionally be aided by improved constraints on how geomorphically effective flows change in width while flowing downstream (Alessio et al., 2021; Neely & DiBiase, 2023) as well as how topographic stresses, which can drive the production of bedrock fractures, modulate hillslope and valley-bottom weathering (e.g., Li & Moon, 2021; Moon et al., 2017; Neely & DiBiase, 2020; Pelletier, 2017; St. Clair et al., 2015), which ultimately impacts landscape morphology.

5.4. Debris-Flow and Fluvial Incision: What do Morphologic Transitions Imply?

We observed that debris-flow incision is dominant at low drainage areas. As drainage area increases, fluvial incision increases until it eventually outpaces erosion by debris flows. This is expected. Importantly, however, we demonstrated that $A_{df} > A_{50}$ across erosion rates (Figure 10), although this observation depends on values of α and β and the method of minimizing misfit between model results and the SGM. Specifically, although we observed that the models for which we minimized the summed misfit ($\alpha = 3$, $\beta = 1$) exhibit A_{50} that approach A_{df} at rapid erosion rates (Figure 10a) and account for nearly 50% of total erosion at A_{df} (Figure 10b), the misfit between these modeled A_{df} and measured A_{df} in the SGM is quite high (Figures 6b and 7a). Therefore, we interpret the more accurately reproduced A_{df} for the models where we minimize misfit to only A_{df} (Figures 8a and 9a) as better capturing A_{50} relative to A_{df} and the debris-flow component of erosion at A_{df} (i.e., $A_{df} > A_{50}$). As such, our results emphasize that morphologic transitions do not necessarily imply a concomitant transition in processes dominance.

Due to the limitations of our model, which we discussed above, we do not fully capture the details of process transitions and how they relate to their morphologic counterparts in steep-lands. We do, however, emphasize that the discrepancy between process and morphologic transition points is intuitive given the nature of the transition from fluvial channels to steep-land valley bottoms. For example, at A_{df} , we often observed that modeled debris flows are responsible for <10% of incision (Figure 10b). Although this proportion seems minor and perhaps unexpected that a morphologic transition corresponds with such a negligible contribution by debris flows, we emphasize that A_{df} denotes the *beginning* of the transition from fluvial channels to steep-land valley bottoms when moving upstream. A_{50} , on the other hand, occurs farther upstream, close to where valley bottoms have become nearly slope-invariant (Figures 10c–10e). As such, although we report single A_{df} values that correspond to a morphologic transition, the morphologic change represented by A_{df} is, indeed, *transitional*. Curved, and therefore transitional, slope-area data were central to the observations of Montgomery and Foufoula-Georgiou (1993) and Stock and Dietrich (2003). Thus, although A_{df} can be conceptualized as a transitional drainage area (and conveniently has units of drainage area), it should not be strictly equated with a discrete process change that separates two separate power laws in slope-area space. Certainly, some landscapes will exhibit more abrupt morphologic transitions than others, and individual steep-land valley bottoms that drain directly into large, high-order fluvial channels do experience an abrupt process transition (Muetting et al., 2021). And as noted by Lavé and Burbank (2004) and DiBiase et al. (2012) in the SGM, debris flows may dominate at low drainage areas and then deposit their sediment farther downstream in larger order fluvial catchments that are periodically emptied by larger floods. In these cases, abrupt transitions from valley bottoms with near-invariant gradients to power-law slope-area scaling

will also reflect sediment supply and transport capacity (Neely & DiBiase, 2023). However, over geologic timescales and averaged across an entire drainage basin, processes will generally exhibit transitions in predominance, particularly when moving along-profile in drainage networks.

6. Conclusions

We investigated the effect of debris flows on steepland evolution. Steep, debris-flow dominated catchments have often been observed to exhibit a characteristic topographic signature in log-log slope-area space, specifically curved slope-area data that transition from near-constant valley-bottom slopes at low drainage areas to power-law scaling at larger drainage areas that is consistent with fluvial incision models. This transition has been suggested to correspond with a process transition from debris-flow to fluvial incision. We observed, in agreement with earlier work, that the sharpness of this transition, as well as the downstream extent of the steepland valley network, varies systematically with uplift rate. We reproduced this relationship between uplift rate and valley morphology, as observed in the SGM, California, by utilizing a 1D landform evolution model that incorporates debris-flow erosion. We performed a series of numerical experiments across a range of uplift rates to constrain parameters in the debris-flow GTL that dictate the importance of valley-bottom slope and debris-flow depth on setting the debris-flow erosion rate. Notably, the model performed best with a strong nonlinear relationship between debris-flow erosion and valley-bottom slope and with a linear to only slightly nonlinear debris-flow erosion dependence on depth.

We used model outputs to identify the drainage area at which debris-flow incision becomes outpaced by fluvial erosion. We found that the drainage area at which this occurs does not correspond with the drainage area associated with the morphologic transition from steepland valley bottoms to fluvial channels. Rather, fluvial erosion begins to become the predominant incision process at drainage areas less than those at which the morphologic transition occurs. While this implies a relatively minor role of debris flows for driving incision relative to fluvial processes near the morphologic transition, the fact that the morphologic transition exists at drainage areas where debris-flow erosion is relatively modest only reinforces the outsized role of debris flows for setting the form of steep landscapes. In other words, debris flows still have a substantial effect on valley morphology even when they are not the dominant erosional process. When moving upstream toward the hillslopes, debris-flow incision increases, highlighting the importance of including debris-flow processes in models of steepland evolution that attempt to reproduce topographic relief, quantify the role of climate and tectonics for setting landscape form, and interpret landscape dynamism, including divide migration and stream capture.

Data Availability Statement

Topographic analysis calculations were completed in MATLAB using TopoToolbox (Schwanghart & Scherler, 2014; <https://github.com/wschwaghart/topotoolbox>). Model and topographic-analysis code are available on HydroShare (Struble et al., 2023; <https://hydroshare.org/resource/f32070149f184e19aa6810d6a8185a5b/>).

Acknowledgments

Paul Alessio, Francis Rengers, an anonymous reviewer, Brian Shiro, and associate editor Jon Pelletier provided detailed and thoughtful comments that greatly improved the quality and scope of this paper. This material is based upon work supported by the National Science Foundation under Grant 1951274 to McGuire and NSF 1951185 to McCoy. Any use of trade, firm, or product names is for descriptive purposes only and does not imply endorsement by the U.S. Government.

References

- Alessio, P., Dunne, T., & Morell, K. (2021). Post-wildfire generation of debris-flow slurry by rill erosion on colluvial hillslopes. *Journal of Geophysical Research: Earth Surface*, 126(11), e2021JF006108. <https://doi.org/10.1029/2021JF006108>
- Almond, P., Roering, J., & Hales, T. C. (2007). Using soil residence time to delineate spatial and temporal patterns of transient landscape response. *Journal of Geophysical Research*, 112(F3), F03S17. <https://doi.org/10.1029/2006JF000568>
- Benda, L. (1990). The influence of debris flows on channels and valley floors in the Oregon Coast Range, USA. *Earth Surface Processes and Landforms*, 15(5), 457–466. <https://doi.org/10.1002/esp.3290150508>
- Bisson, P. A., Montgomery, D. R., & Buffington, J. M. (2006). Valley segments, stream reaches, and channel units. In F. R. Hauer, & G. A. Lamberti (Eds.), *Methods in stream ecology* (Vol. 1, pp. 21–47). Elsevier. <https://doi.org/10.1016/B978-0-12-416558-8.00002-0>
- Blythe, A. E., Burbank, D. W., Farley, K. A., & Fielding, E. J. (2000). Structural and topographic evolution of the central Transverse Ranges, California, from apatite fission-track, (U-Th)/He and digital elevation model analyses: Evolution of the central Transverse Ranges, California. *Basin Research*, 12(2), 97–114. <https://doi.org/10.1046/j.1365-2117.2000.00116.x>
- Campforts, B., Shobe, C. M., Overeem, I., & Tucker, G. E. (2022). The art of landslides: How stochastic mass wasting shapes topography and influences landscape dynamics. *Journal of Geophysical Research: Earth Surface*, 127(8), e2022JF006745. <https://doi.org/10.1029/2022JF006745>
- Cannon, S. H. (2001). Debris-flow generation from recently burned watersheds. *Environmental and Engineering Geoscience*, 7(4), 321–341. <https://doi.org/10.2113/gsegeosci.7.4.321>
- Clubb, F. J., Mudd, S. M., Attal, M., Milodowski, D. T., & Grieve, S. W. D. (2016). The relationship between drainage density, erosion rate, and hilltop curvature: Implications for sediment transport processes. *Journal of Geophysical Research: Earth Surface*, 121(10), 1724–1745. <https://doi.org/10.1002/2015JF003747>

- Clubb, F. J., Mudd, S. M., Milodowski, D. T., Hurst, M. D., & Slater, L. J. (2014). Objective extraction of channel heads from high-resolution topographic data. *Water Resources Research*, 50(5), 4283–4304. <https://doi.org/10.1002/2013WR015167>
- Cook, K. L., Turowski, J. M., & Hovius, N. (2013). A demonstration of the importance of bedload transport for fluvial bedrock erosion and knickpoint propagation. *Earth Surface Processes and Landforms*, 38(7), 683–695. <https://doi.org/10.1002/esp.3313>
- Crosby, B. T., & Whipple, K. X. (2006). Knickpoint initiation and distribution within fluvial networks: 236 waterfalls in the Waipaoa River, North Island, New Zealand. *Geomorphology*, 82(1–2), 16–38. <https://doi.org/10.1016/j.geomorph.2005.08.023>
- DiBiase, R. A., Heimsath, A. M., & Whipple, K. X. (2012). Hillslope response to tectonic forcing in threshold landscapes. *Earth Surface Processes and Landforms*, 37(8), 855–865. <https://doi.org/10.1002/esp.3205>
- DiBiase, R. A., & Lamb, M. P. (2020). Dry sediment loading of headwater channels fuels post-wildfire debris flows in bedrock landscapes. *Geology*, 48(2), 189–193. <https://doi.org/10.1130/G46847.1>
- DiBiase, R. A., & Whipple, K. X. (2011). The influence of erosion thresholds and runoff variability on the relationships among topography, climate, and erosion rate. *Journal of Geophysical Research*, 116(F4), F04036. <https://doi.org/10.1029/2011JF002095>
- DiBiase, R. A., Whipple, K. X., Heimsath, A. M., & Ouimet, W. B. (2010). Landscape form and millennial erosion rates in the San Gabriel Mountains, CA. *Earth and Planetary Science Letters*, 289(1–2), 134–144. <https://doi.org/10.1016/j.epsl.2009.10.036>
- DiBiase, R. A., Whipple, K. X., Lamb, M. P., & Heimsath, A. M. (2015). The role of waterfalls and knickzones in controlling the style and pace of landscape adjustment in the western San Gabriel Mountains, California. *Geological Society of America Bulletin*, 127(3–4), 539–559. <https://doi.org/10.1130/B31113.1>
- Dietrich, W. E., Bellugi, D. G., Sklar, L. S., Stock, J. D., Heimsath, A. M., & Roering, J. J. (2003). Geomorphic transport laws for predicting landscape form and dynamics. In P. R. Wilcock, & R. M. Iverson (Eds.), *Prediction in geomorphology, geophysical monograph series* (Vol. 135, pp. 103–132). American Geophysical Union. <https://doi.org/10.1029/135GM09>
- Gabet, E. J., Mudd, S. M., Wood, R. W., Grieve, S. W. D., Binnie, S. A., & Dunai, T. J. (2021). Hilltop curvature increases with the square root of erosion rate. *Journal of Geophysical Research: Earth Surface*, 126(5), e2020JF005858. <https://doi.org/10.1029/2020JF005858>
- Gartner, J. E., Cannon, S. H., & Santi, P. M. (2014). Empirical models for predicting volumes of sediment deposited by debris flows and sediment-laden floods in the transverse ranges of southern California. *Engineering Geology*, 176, 45–56. <https://doi.org/10.1016/j.enggeo.2014.04.008>
- Gartner, J. E., Cannon, S. H., Santi, P. M., & Dewolfe, V. G. (2008). Empirical models to predict the volumes of debris flows generated by recently burned basins in the western U.S. *Geomorphology*, 96(3–4), 339–354. <https://doi.org/10.1016/j.geomorph.2007.02.033>
- Gilbert, G. K. (1877). Report on the geology of the Henry Mountains. U.S. Geographical and Geological Survey Report. 160. 5 plates. <https://doi.org/10.3133/70039916>
- Gilbert, G. K. (1909). The convexity of hilltops. *The Journal of Geology*, 17(4), 344–350. <https://doi.org/10.1086/621620>
- Gorr, A. N., McGuire, L. A., Youberg, A. M., & Rengers, F. K. (2022). A progressive flow-routing model for rapid assessment of debris-flow inundation. *Landslides*, 19(9), 2055–2073. <https://doi.org/10.1007/s10346-022-01890-y>
- Grieve, S. W. D., Mudd, S. M., & Hurst, M. D. (2016). How long is a hillslope? *Earth Surface Processes and Landforms*, 41(8), 1039–1054. <https://doi.org/10.1002/esp.3884>
- Groh, E. L., & Scheingross, J. S. (2021). Morphologic signatures of autogenic waterfalls: A case study in the San Gabriel Mountains, California. *Geology*, 50(2), 248–253. <https://doi.org/10.1130/G49320.1>
- Guilinger, J. J., Gray, A. B., Barth, N. C., & Fong, B. T. (2020). The evolution of sediment sources over a sequence of postfire sediment-laden flows revealed through repeat high-resolution change detection. *Journal of Geophysical Research: Earth Surface*, 125(10), e2020JF005527. <https://doi.org/10.1029/2020JF005527>
- Heimsath, A. M., DiBiase, R. A., & Whipple, K. X. (2012). Soil production limits and the transition to bedrock-dominated landscapes. *Nature Geoscience*, 5(3), 210–214. <https://doi.org/10.1038/ngeo1380>
- Heimsath, A. M., Dietrich, W. E., Nishiizumi, K., & Finkel, R. C. (2001). Stochastic processes of soil production and transport: Erosion rates, topographic variation and cosmogenic nuclides in the Oregon Coast Range. *Earth Surface Processes and Landforms*, 26(5), 531–552. <https://doi.org/10.1002/esp.209>
- Hergarten, S., Robl, J., & Stüwe, K. (2016). Tectonic geomorphology at small catchment sizes—Extensions of the stream-power approach and the χ method. *Earth Surface Dynamics*, 4(1), 1–9. <https://doi.org/10.5194/esurf-4-1-2016>
- Hilley, G. E., Porder, S., Aron, F., Baden, C. W., Johnstone, S. A., Liu, F., et al. (2019). Earth's topographic relief potentially limited by an upper bound on channel steepness. *Nature Geoscience*, 12(10), 828–832. <https://doi.org/10.1038/s41561-019-0442-3>
- Howard, A. D. (1994). A detachment-limited model of drainage basin evolution. *Water Resources Research*, 30(7), 2261–2285. <https://doi.org/10.1029/94WR00757>
- Hsu, L., Dietrich, W. E., & Sklar, L. S. (2008). Experimental study of bedrock erosion by granular flows. *Journal of Geophysical Research*, 113(F2), F02001. <https://doi.org/10.1029/2007JF000778>
- Hsu, L., Dietrich, W. E., & Sklar, L. S. (2014). Mean and fluctuating basal forces generated by granular flows: Laboratory observations in a large vertically rotating drum. *Journal of Geophysical Research: Earth Surface*, 119(6), 1283–1309. <https://doi.org/10.1002/2013JF003078>
- Hurst, M. D., Grieve, S. W. D., Clubb, F. J., & Mudd, S. M. (2019). Detection of channel-hillslope coupling along a tectonic gradient. *Earth and Planetary Science Letters*, 522, 30–39. <https://doi.org/10.1016/j.epsl.2019.06.018>
- Hurst, M. D., Mudd, S. M., Walcott, R., Attal, M., & Yoo, K. (2012). Using hilltop curvature to derive the spatial distribution of erosion rates. *Journal of Geophysical Research*, 117(F2), F02017. <https://doi.org/10.1029/2011JF002057>
- Iverson, R. M. (1997). The physics of debris flows. *Reviews of Geophysics*, 35(3), 245–296. <https://doi.org/10.1029/97RG00426>
- Kean, J. W., McCoy, S. W., Tucker, G. E., Staley, D. M., & Coe, J. A. (2013). Runoff-generated debris flows: Observations and modeling of surge initiation, magnitude, and frequency. *Journal of Geophysical Research: Earth Surface*, 118(4), 2190–2207. <https://doi.org/10.1002/jgrf.20148>
- Kean, J. W., McGuire, L. A., Rengers, F. K., Smith, J. B., & Staley, D. M. (2016). Amplification of postwildfire peak flow by debris: Amplification of postwildfire peak flow. *Geophysical Research Letters*, 43(16), 8545–8553. <https://doi.org/10.1002/2016GL069661>
- Kean, J. W., Staley, D. M., & Cannon, S. H. (2011). In situ measurements of post-fire debris flows in southern California: Comparisons of the timing and magnitude of 24 debris-flow events with rainfall and soil moisture conditions. *Journal of Geophysical Research*, 116(F4), F04019. <https://doi.org/10.1029/2011JF002005>
- Kirby, E., & Whipple, K. (2001). Quantifying differential rock-uplift rates via stream profile analysis. *Geology*, 29(5), 415–418. [https://doi.org/10.1130/0091-7613\(2001\)029<0415:QDRURV>2.0.CO;2](https://doi.org/10.1130/0091-7613(2001)029<0415:QDRURV>2.0.CO;2)
- Kirby, E., & Whipple, K. X. (2012). Expression of active tectonics in erosional landscapes. *Journal of Structural Geology*, 44, 54–75. <https://doi.org/10.1016/j.jsg.2012.07.009>
- Lague, D. (2014). The stream power river incision model: Evidence, theory and beyond. *Earth Surface Processes and Landforms*, 39(1), 38–61. <https://doi.org/10.1002/esp.3462>

- Lague, D., & Davy, P. (2003). Constraints on the long-term colluvial erosion law by analyzing slope-area relationships at various tectonic uplift rates in the Siwaliks Hills (Nepal). *Journal of Geophysical Research*, *108*(B2), 2129. <https://doi.org/10.1029/2002JB001893>
- Lai, L. S., Roering, J. J., Finnegan, N. J., Dorsey, R. J., & Yen, J. (2021). Coarse sediment supply sets the slope of bedrock channels in rapidly uplifting terrain: Field and topographic evidence from eastern Taiwan. *Earth Surface Processes and Landforms*, *46*(13), 2671–2689. <https://doi.org/10.1002/esp.5200>
- Lamb, M. P., Dietrich, W. E., & Venditti, J. G. (2008). Is the critical Shields stress for incipient sediment motion dependent on channel-bed slope? *Journal of Geophysical Research*, *113*(F2), F02008. <https://doi.org/10.1029/2007JF000831>
- Lamb, M. P., Scheingross, J. S., Amidon, W. H., Swanson, E., & Limaye, A. (2011). A model for fire-induced sediment yield by dry ravel in steep landscapes. *Journal of Geophysical Research*, *116*(F3), F03006. <https://doi.org/10.1029/2010JF001878>
- Larsen, I. J., & Montgomery, D. R. (2012). Landslide erosion coupled to tectonics and river incision. *Nature Geoscience*, *5*(7), 468–473. <https://doi.org/10.1038/ngeo1479>
- Lashermes, B., Foufoula-Georgiou, E., & Dietrich, W. E. (2007). Channel network extraction from high resolution topography using wavelets. *Geophysical Research Letters*, *34*(23), L23S04. <https://doi.org/10.1029/2007GL031140>
- Lavé, J., & Burbank, D. (2004). Denudation processes and rates in the Transverse Ranges, southern California: Erosional response of a transitional landscape to external and anthropogenic forcing. *Journal of Geophysical Research*, *109*(F1), F01006. <https://doi.org/10.1029/2003JF000023>
- Li, G. K., & Moon, S. (2021). Topographic stress control on bedrock landslide size. *Nature Geoscience*, *14*(5), 307–313. <https://doi.org/10.1038/s41561-021-00739-8>
- May, C., Roering, J., Eaton, L. S., & Burnett, K. M. (2013). Controls on valley width in mountainous landscapes: The role of landsliding and implications for salmonid habitat. *Geology*, *41*(4), 503–506. <https://doi.org/10.1130/G33979.1>
- McCoy, S. W. (2015). Research focus: Infrequent, large-magnitude debris flows are important agents of landscape change. *Geology*, *43*(5), 463–464. <https://doi.org/10.1130/focus052015.1>
- McCoy, S. W., Kean, J. W., Coe, J. A., Staley, D. M., Wasklewicz, T. A., & Tucker, G. E. (2010). Evolution of a natural debris flow: In situ measurements of flow dynamics, video imagery, and terrestrial laser scanning. *Geology*, *38*(8), 735–738. <https://doi.org/10.1130/G30928.1>
- McCoy, S. W., Tucker, G. E., Kean, J. W., & Coe, J. A. (2013). Field measurement of basal forces generated by erosive debris flows. *Journal of Geophysical Research: Earth Surface*, *118*(2), 589–602. <https://doi.org/10.1002/jgrf.20041>
- McGuire, L. A., McCoy, S. W., Marc, O., Struble, W., & Barnhart, K. R. (2022). Steady-state forms of channel profiles shaped by debris-flow and fluvial processes. *Earth Surface Dynamics Discussions*, <https://doi.org/10.5194/esurf-2022-47>
- McGuire, L. A., Rengers, F. K., Kean, J. W., & Staley, D. M. (2017). Debris flow initiation by runoff in a recently burned basin: Is grain-by-grain sediment bulking or en masse failure to blame? *Geophysical Research Letters*, *44*(14), 7310–7319. <https://doi.org/10.1002/2017GL074243>
- Montgomery, D. R. (2001). Slope distributions, threshold hillslopes, and steady-state topography. *American Journal of Science*, *301*(4–5), 432–454. <https://doi.org/10.2475/ajs.301.4-5.432>
- Montgomery, D. R., & Foufoula-Georgiou, E. (1993). Channel network source representation using digital elevation models. *Water Resources Research*, *29*(12), 3925–3934. <https://doi.org/10.1029/93WR02463>
- Montgomery, D. R., & Gran, K. B. (2001). Downstream variations in the width of bedrock channels. *Water Resources Research*, *37*(6), 1841–1846. <https://doi.org/10.1029/2000WR900393>
- Moon, S., Perron, J. T., Martel, S. J., Holbrook, W. S., & St. Clair, J. (2017). A model of three-dimensional topographic stresses with implications for bedrock fractures, surface processes, and landscape evolution. *Journal of Geophysical Research: Earth Surface*, *122*(4), 823–846. <https://doi.org/10.1002/2016JF004155>
- Morton, D. M., & Miller, F. K. (2006). Geologic map of the San Bernardino and Santa Ana 30' x 60' quadrangles, California. U.S. Geological Survey Open-File Report 2006-1217. 194. 4 sheets. <https://doi.org/10.3133/ofr20061217>
- Mudd, S. M. (2017). Detection of transience in eroding landscapes: Detection of transience in eroding landscapes. *Earth Surface Processes and Landforms*, *42*(1), 24–41. <https://doi.org/10.1002/esp.3923>
- Mudd, S. M., & Furbish, D. J. (2007). Responses of soil-mantled hillslopes to transient channel incision rates. *Journal of Geophysical Research*, *112*(F3), F03S18. <https://doi.org/10.1029/2006JF000516>
- Mueting, A., Bookhagen, B., & Strecker, M. R. (2021). Identification of debris-flow channels using high-resolution topographic data: A case study in the Quebrada del Toro, NW Argentina. *Journal of Geophysical Research: Earth Surface*, *126*(12), e2021JF006330. <https://doi.org/10.1029/2021JF006330>
- Neely, A. B., & DiBiase, R. A. (2020). Drainage area, bedrock fracture spacing, and weathering controls on landscape-scale patterns in surface sediment grain size. *Journal of Geophysical Research: Earth Surface*, *125*(10), e2020JF005560. <https://doi.org/10.1029/2020JF005560>
- Neely, A. B., & DiBiase, R. A. (2023). Sediment controls on the transition from debris flow to fluvial channels in steep mountain ranges. *Earth Surface Processes and Landforms*, *48*(7), 20. <https://doi.org/10.1002/esp.5553>
- Neely, A. B., DiBiase, R. A., Corbett, L. B., Bierman, P. R., & Caffee, M. W. (2019). Bedrock fracture density controls on hillslope erodibility in steep, rocky landscapes with patchy soil cover, southern California, USA. *Earth and Planetary Science Letters*, *522*, 186–197. <https://doi.org/10.1016/j.epsl.2019.06.011>
- Ouimet, W. B., Whipple, K. X., & Granger, D. E. (2009). Beyond threshold hillslopes: Channel adjustment to base-level fall in tectonically active mountain ranges. *Geology*, *37*(7), 579–582. <https://doi.org/10.1130/G30013A.1>
- Palucis, M. C., Ulizio, T. P., & Lamb, M. P. (2021). Debris flow initiation from ravel-filled channel bed failure following wildfire in a bedrock landscape with limited sediment supply. *Geological Society of America Bulletin*, *133*(9–10), 2079–2096. <https://doi.org/10.1130/B35822.1>
- Parson, A., Robichaud, P. R., Lewis, S. A., Napper, C., & Clark, J. T. (2010). *Field guide for mapping post-fire soil burn severity*. General Technical Report RMRS-GTR-243. (pp. 49). U.S. Department of Agriculture, Forest Service, Rocky Mountain Research Station: Ft. Collins, CO. <https://doi.org/10.2737/RMRS-GTR-243>
- Passalacqua, P., Do Trung, T., Foufoula-Georgiou, E., Sapiro, G., & Dietrich, W. E. (2010). A geometric framework for channel network extraction from lidar: Nonlinear diffusion and geodesic paths. *Journal of Geophysical Research*, *115*(F1), F01002. <https://doi.org/10.1029/2009JF001254>
- Pelletier, J. D. (2013). A robust, two-parameter method for the extraction of drainage networks from high-resolution digital elevation models (DEMs): Evaluation using synthetic and real-world DEMs. *Water Resources Research*, *49*(1), 75–89. <https://doi.org/10.1029/2012WR012452>
- Pelletier, J. D. (2017). Quantifying the controls on potential soil production rates: A case study of the San Gabriel Mountains, California. *Earth Surface Dynamics*, *5*(3), 479–492. <https://doi.org/10.5194/esurf-5-479-2017>
- Pelletier, J. D., Nichols, M. H., & Nearing, M. A. (2016). The influence of Holocene vegetation changes on topography and erosion rates: A case study at Walnut Gulch Experimental Watershed, Arizona. *Earth Surface Dynamics*, *4*(2), 471–488. <https://doi.org/10.5194/esurf-4-471-2016>
- Penseri, B. D., Roering, J. J., & Streig, A. (2017). A morphologic proxy for debris flow erosion with application to the earthquake deformation cycle, Cascadia Subduction Zone, USA. *Geomorphology*, *282*, 150–161. <https://doi.org/10.1016/j.geomorph.2017.01.018>

- Perron, J. T., Dietrich, W. E., & Kirchner, J. W. (2008). Controls on the spacing of first-order valleys. *Journal of Geophysical Research*, *113*(F4), F04016. <https://doi.org/10.1029/2007JF000977>
- Petersen, M. D., & Wesnousky, S. G. (1994). Fault slip rates and earthquake histories for active faults in southern California. *Bulletin of the Seismological Society of America*, *84*(5), 1608–1649. <https://doi.org/10.1785/BSSA0840051608>
- Prancevic, J. P., Lamb, M. P., & Fuller, B. M. (2014). Incipient sediment motion across the river to debris-flow transition. *Geology*, *42*(3), 191–194. <https://doi.org/10.1130/G34927.1>
- PRISM Climate Group. (2021). *Parameter-elevation regressions on independent slopes model (PRISM) climate Group*. [WWW Document]. PRISM Climate Group: Oregon State University. Retrieved from <https://prism.oregonstate.edu/>
- Recking, A. (2009). Theoretical development on the effects of changing flow hydraulics on incipient bed load motion. *Water Resources Research*, *45*(4), W04401. <https://doi.org/10.1029/2008WR006826>
- Reneau, S. L., & Dietrich, W. E. (1991). Erosion rates in the southern Oregon Coast Range: Evidence for an equilibrium between hillslope erosion and sediment yield. *Earth Surface Processes and Landforms*, *16*(4), 307–322. <https://doi.org/10.1002/esp.3290160405>
- Rengers, F. K., McGuire, L. A., Kean, J. W., Staley, D. M., Dobre, M., Robichaud, P. R., & Swetnam, T. (2021). Movement of sediment through a burned landscape: Sediment volume observations and model comparisons in the San Gabriel Mountains, California, USA. *Journal of Geophysical Research: Earth Surface*, *126*(7), e2020JF006053. <https://doi.org/10.1029/2020JF006053>
- Rengers, F. K., McGuire, L. A., Oakley, N. S., Kean, J. W., Staley, D. M., & Tang, H. (2020). Landslides after wildfire: Initiation, magnitude, and mobility. *Landslides*, *17*(11), 2631–2641. <https://doi.org/10.1007/s10346-020-01506-3>
- Rickenmann, D. (1999). Empirical relationships for debris flows. *Natural Hazards*, *19*(1), 47–77. <https://doi.org/10.1023/A:1008064220727>
- Roering, J. J. (2008). How well can hillslope evolution models “explain” topography? Simulating soil transport and production with high-resolution topographic data. *Geological Society of America Bulletin*, *120*(9–10), 1248–1262. <https://doi.org/10.1130/B26283.1>
- Roering, J. J., Kirchner, J. W., & Dietrich, W. E. (1999). Evidence for nonlinear, diffusive sediment transport on hillslopes and implications for landscape morphology. *Water Resources Research*, *35*(3), 853–870. <https://doi.org/10.1029/1998WR900090>
- Roering, J. J., Kirchner, J. W., & Dietrich, W. E. (2001). Hillslope evolution by nonlinear, slope-dependent transport: Steady state morphology and equilibrium adjustment timescales. *Journal of Geophysical Research*, *106*(B8), 16499–16513. <https://doi.org/10.1029/2001JB000323>
- Roering, J. J., Perron, J. T., & Kirchner, J. W. (2007). Functional relationships between denudation and hillslope form and relief. *Earth and Planetary Science Letters*, *264*(1–2), 245–258. <https://doi.org/10.1016/j.epsl.2007.09.035>
- Santi, P. M., de Wolfe, V. G., Higgins, J. D., Cannon, S. H., & Gartner, J. E. (2008). Sources of debris flow material in burned areas. *Geomorphology*, *96*(3–4), 310–321. <https://doi.org/10.1016/j.geomorph.2007.02.022>
- Santi, P. M., & Morandi, L. (2013). Comparison of debris-flow volumes from burned and unburned areas. *Landslides*, *10*(6), 757–769. <https://doi.org/10.1007/s10346-012-0354-4>
- Schanz, S. A., & Montgomery, D. R. (2016). Lithologic controls on valley width and strath terrace formation. *Geomorphology*, *258*, 58–68. <https://doi.org/10.1016/j.geomorph.2016.01.015>
- Schmidt, K. M., Roering, J. J., Stock, J. D., Dietrich, W. E., Montgomery, D. R., & Schaub, T. (2001). The variability of root cohesion as an influence on shallow landslide susceptibility in the Oregon Coast Range. *Canadian Geotechnical Journal*, *38*(5), 995–1024. <https://doi.org/10.1139/t01-031>
- Schwanghart, W., & Scherler, D. (2014). Short communication: TopToolbox 2—MATLAB-based software for topographic analysis and modeling in Earth surface sciences. *Earth Surface Dynamics*, *2*, 1–7. <https://doi.org/10.5194/esurf-2-1-2014>
- Schwanghart, W., & Scherler, D. (2020). Divide mobility controls knickpoint migration on the Roan Plateau (Colorado, USA). *Geology*, *48*(7), 698–702. <https://doi.org/10.1130/G47054.1>
- Shelef, E., & Hilley, G. E. (2016). A unified framework for modeling landscape evolution by discrete flows. *Journal of Geophysical Research: Earth Surface*, *121*(5), 816–842. <https://doi.org/10.1002/2015JF003693>
- Silbert, L. E., Ertas, D., Grest, G. S., Halsey, T. C., Levine, D., & Plimpton, S. J. (2001). Granular flow down an inclined plane: Bagnold scaling and rheology. *Physical Review E*, *64*(5), 051302. <https://doi.org/10.1103/PhysRevE.64.051302>
- Sklar, L. S., & Dietrich, W. E. (2001). Sediment and rock strength controls on river incision into bedrock. *Geology*, *29*(12), 1087–1090. [https://doi.org/10.1130/0091-7613\(2001\)029<1087:SARSCO>2.0.CO;2](https://doi.org/10.1130/0091-7613(2001)029<1087:SARSCO>2.0.CO;2)
- Sklar, L. S., & Dietrich, W. E. (2004). A mechanistic model for river incision into bedrock by saltating bed load. *Water Resources Research*, *40*(6), W06301. <https://doi.org/10.1029/2003WR002496>
- Spotila, J. A., House, M. A., Blythe, A. E., Niemi, N. A., & Bank, G. C. (2002). Controls on the erosion and geomorphic evolution of the San Bernardino and San Gabriel Mountains, southern California. In A. Barth (Ed.), *Contributions to crustal evolution of the southwestern United States. Geological Society of America special paper 365* (pp. 205–230). Geological Society of America. <https://doi.org/10.1130/0-8137-2365-5.205>
- Staley, D. M., Kean, J. W., & Rengers, F. K. (2020). The recurrence interval of post-fire debris-flow generating rainfall in the southwestern United States. *Geomorphology*, *370*, 107392. <https://doi.org/10.1016/j.geomorph.2020.107392>
- Staley, D. M., Negri, J. A., Kean, J. W., Laber, J. L., Tillery, A. C., & Youberg, A. M. (2017). Prediction of spatially explicit rainfall intensity–duration thresholds for post-fire debris-flow generation in the western United States. *Geomorphology*, *278*, 149–162. <https://doi.org/10.1016/j.geomorph.2016.10.019>
- Staley, D. M., Wasklewicz, T. A., & Kean, J. W. (2014). Characterizing the primary material sources and dominant erosional processes for post-fire debris-flow initiation in a headwater basin using multi-temporal terrestrial laser scanning data. *Geomorphology*, *214*, 324–338. <https://doi.org/10.1016/j.geomorph.2014.02.015>
- St. Clair, J., Moon, S., Holbrook, W. S., Perron, J. T., Riebe, C. S., Martel, S. J., et al. (2015). Geophysical imaging reveals topographic stress control of bedrock weathering. *Science*, *350*(6260), 534–538. <https://doi.org/10.1126/science.122210>
- Stock, J., & Dietrich, W. E. (2003). Valley incision by debris flows: Evidence of a topographic signature. *Water Resources Research*, *39*(4), 1089. <https://doi.org/10.1029/2001WR001057>
- Stock, J. D., & Dietrich, W. E. (2006). Erosion of steepland valleys by debris flows. *Geological Society of America Bulletin*, *118*(9–10), 1125–1148. <https://doi.org/10.1130/B25902.1>
- Stock, J. D., Montgomery, D. R., Collins, B. D., Dietrich, W. E., & Sklar, L. (2005). Field measurements of incision rates following bedrock exposure: Implications for process controls on the long profiles of valleys cut by rivers and debris flows. *Geological Society of America Bulletin*, *117*(1–2), 174–194. <https://doi.org/10.1130/B25560.1>
- Struble, W. T., McGuire, L. A., McCoy, S. W., Barnhart, K. R., & Marc, O. (2023). Steepland topographic analysis and landform evolution modeling including an incorporated debris-flow process law for the San Gabriel Mountains, California [Software]. Hydroshare. <https://hydroshare.org/resource/f32070149f184e19aa6810d6a8185a5b/>
- Struble, W. T., & Roering, J. J. (2021). Hilltop curvature as a proxy for erosion rate: Wavelets enable rapid computation and reveal systematic underestimation. *Earth Surface Dynamics*, *9*(5), 1279–1300. <https://doi.org/10.5194/esurf-9-1279-2021>

- Swanson, F. J. (1981). Fire and geomorphic processes. In H. A. Mooney, T. M. Bonnicksen, N. L. Christensen Jr., J. E. Lotan, & W. A. Reiners (Eds.), *Fire regime and ecosystem properties, general technical report WO-GTR-26* (pp. 401–421). U.S. Department of Agriculture, Forest Service.
- Sweeney, K. E., Roering, J. J., Almond, P., & Reckling, T. (2012). How steady are steady-state landscapes? Using visible–near-infrared soil spectroscopy to quantify erosional variability. *Geology*, *40*(9), 807–810. <https://doi.org/10.1130/G33167.1>
- Tomkin, J. H., Brandon, M. T., Pazzaglia, F. J., Barbour, J. R., & Willett, S. D. (2003). Quantitative testing of bedrock incision models for the Clearwater River, NW Washington State. *Journal of Geophysical Research*, *108*(B6), 2308. <https://doi.org/10.1029/2001JB000862>
- Townsend, K. F., Clark, M. K., & Zekkos, D. (2021). Profiles of near-surface rock mass strength across gradients in burial, erosion, and time. *Journal of Geophysical Research: Earth Surface*, *126*(4), e2020JF005694. <https://doi.org/10.1029/2020JF005694>
- Turowski, J. M. (2021). Upscaling sediment-flux-dependent fluvial bedrock incision to long timescales. *Journal of Geophysical Research: Earth Surface*, *126*(5), e2020JF005880. <https://doi.org/10.1029/2020JF005880>
- Turowski, J. M., Hovius, N., Meng-Long, H., Lague, D., & Men-Chiang, C. (2008). Distribution of erosion across bedrock channels. *Earth Surface Processes and Landforms*, *33*(3), 353–363. <https://doi.org/10.1002/esp.1559>
- U.S. Department of Agriculture (USDA) Forest Service. (2022). BAER imagery support data download. [WWW Document]. Retrieved from <https://fsapps.nwcg.gov/baer/baer-imagery-support-data-download>
- U.S. Geological Survey. (2019). 3D elevation program 1/3 arc-second resolution digital elevation model (published 20190919). [WWW Document]. Retrieved from <https://apps.nationalmap.gov/downloader/>
- Wall, S., Murphy, B. P., Belmont, P., & Yocom, L. (2022). Predicting post-fire debris flow grain sizes and depositional volumes in the Intermountain West, United States. *Earth Surface Processes and Landforms*, *48*(1), 179–197. <https://doi.org/10.1002/esp.5480>
- Whipple, K. X., & Tucker, G. E. (1999). Dynamics of the stream-power river incision model: Implications for height limits of mountain ranges, landscape response timescales, and research needs. *Journal of Geophysical Research*, *104*(B8), 17661–17674. <https://doi.org/10.1029/1999JB900120>
- Whittaker, A. C. (2012). How do landscapes record tectonics and climate? *Lithosphere*, *4*(2), 160–164. <https://doi.org/10.1130/RF.L003.1>
- Willett, S. D., McCoy, S. W., Perron, J. T., Goren, L., & Chen, C.-Y. (2014). Dynamic reorganization of river basins. *Science*, *343*(6175), 1248765. <https://doi.org/10.1126/science.1248765>
- Wobus, C., Whipple, K. X., Kirby, E., Snyder, N., Johnson, J., Spyropoulos, K., et al. (2006). Tectonics from topography: Procedures, promise, and pitfalls. In S. D. Willett, N. Hovius, M. T. Brandon, & D. M. Fisher (Eds.), *Tectonics, climate, and landscape evolution. Geological society of America special paper 398* (pp. 55–74). Geological Society of America. [https://doi.org/10.1130/2006.2398\(04\)](https://doi.org/10.1130/2006.2398(04))
- Yanites, B. J. (2018). The dynamics of channel slope, width, and sediment in actively eroding bedrock river systems. *Journal of Geophysical Research: Earth Surface*, *123*(7), 1504–1527. <https://doi.org/10.1029/2017JF004405>
- Yerkes, R. F., & Campbell, R. H. (2005). *Preliminary geologic map of the Los Angeles 30' x 60' quadrangle*. U.S. Geological Survey Open-File Report 2005-1019. <https://doi.org/10.3133/ofr20051019>